



## Research Paper

## Highly efficient iodine capture and ultrafast fluorescent detection of heavy metals using PANI/LDH@CNT nanocomposite



Mansour A.S. Salem<sup>a,b,\*</sup>, Amjad Mumtaz Khan<sup>a,\*\*</sup>, Yahiya Kadaf Manea<sup>b</sup>, Mohsen T.A. Qashqoosh<sup>b</sup>, Faiza A.M. Alahdal<sup>a</sup>

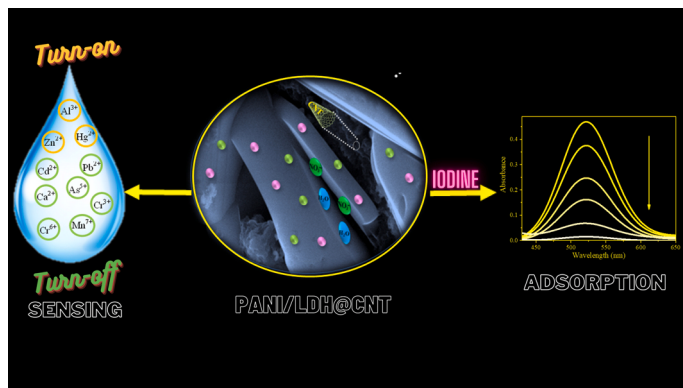
<sup>a</sup> Department of Chemistry, Aligarh Muslim University, Aligarh 202002, India

<sup>b</sup> Department of Chemistry, University of Aden, Aden, Yemen

## HIGHLIGHTS

## GRAPHICAL ABSTRACT

- Ex-situ oxidative polymerization was used to synthesize PANI/LDH@CNT.
- The adsorption capacity for  $I_{2(aq)}$  was  $303.20 \text{ mg g}^{-1}$  and  $900 \text{ mg g}^{-1}$  in  $I_{2(\text{vap})}$ .
- PANI/LDH@CNT showed a high sensitivity for heavy metal ions detection at ppb levels.



## ARTICLE INFO

Editor: Sungjun Bae

## Keywords:

Carbon nanotubes  
Adsorption  
CHEF effect  
Fluorescent probe

## ABSTRACT

Here, the hybrid material of polyaniline/layered double hydroxide@carbonnanotubes (PANI/LDH@CNT) is considered a multifunctional material. Instrumental methods, including FTIR, XRD, TEM, SEM, and TGA/DTA were utilized to characterize PANI/LDH@CNT. The polymerization method created PANI/LDH@CNT as an adsorbent to remove toxic iodine in hexane solution with a capture capacity of  $303.20 \text{ mg g}^{-1}$  during 9 h. It is  $900 \text{ mg g}^{-1}$  in the vapor phase within 24 h. After three cycles, the PANI/LDH@CNT could be regenerated while maintaining 91.90 % iodine adsorption efficiency. Due to the presence of free amine (-N) groups, OH<sup>-</sup>, CO<sub>2</sub>H, and π-π conjugated structures in the PANI/LDH@CNT, it is also explored for efficient iodine uptake. It was demonstrated that the pseudo-first-order (PFO) and Langmuir model had the optimum correlation with the kinetic and isotherm data, respectively. Moreover, the use of PANI/LDH@CNT is not only limited to iodine capture; it can also be utilized as a sensitive sensor that displays a fluorescence "turn-off" response for Mn<sup>7+</sup> and Cr<sup>6+</sup> ions and a fluorescence "turn-on" response in the case of Al<sup>3+</sup> ions. The fluorescence intensity of the PANI/LDH@CNT was turned off in the presence of Mn<sup>7+</sup> and Cr<sup>6+</sup> because of the fluorescence inner filter effect (IFE) mechanism. In contrast, the fluorescence intensity was turned on in the case of Al<sup>3+</sup>, relying on the chelation-

\* Corresponding author at: Department of Chemistry, Aligarh Muslim University, Aligarh 202002, India.

\*\* Corresponding author.

E-mail addresses: mansouras2023@gmail.com (M.A.S. Salem), amjadmtkhan96@gmail.com (A.M. Khan).

enhanced fluorescence (CHEF) effect mechanism. Under optimal conditions, the limit of detection (LOD) of 51, 59, and 81 nM for Mn<sup>7+</sup>, Cr<sup>6+</sup>, and Al<sup>3+</sup>, respectively. According to the literature, this is probably the first example based on PANI/LDH@CNT as a multifunctional hybrid material employed as an adsorbent for capturing radioactive iodine and as a chemosensor for detecting heavy metal ions in aqueous solutions.

## 1. Introduction

Water pollution by heavy metal ions is a significant environmental issue because of its non-biodegradability and bioaccumulation in the surrounding environment and humans [20,43]. Manganese (Mn<sup>7+</sup>) is among heavy metal pollutants, a vital trace nutrient in all living systems, and plays various significant biological roles. World Health Organization (WHO) recommends a guideline value of 0.4 mg L<sup>-1</sup> for Mn<sup>7+</sup> in drinking water [2]. Any variation in manganese concentration levels might cause central nervous system problems, resulting in severe symptoms like muscular pain, hallucinations, mental irritability, sleep disturbances, fatigability, hypertonia, gait changes, and leading to Parkinson's disease. On the other hand, its heavy metal characteristic and substantial oxidation property make it a carcinogenic and toxic species in water consumed by humans and recycling systems. In industry, Mn<sup>7+</sup> has been used as a potent oxidation agent, generating large amounts of toxic wastewater. Manganese ions have contributed to severe pollution, causing damage to plants and contaminating drinking water. Therefore, Mn<sup>7+</sup> has recently attracted much attention among pollutants, and detecting Mn<sup>7+</sup> is vital for environmental protection [20,46,54,65,66,76].

Similarly, in soil, groundwater, and saltwater, chromium is often found in two oxidation states, chromium (III) (Cr<sup>3+</sup>) and chromium (VI) (Cr<sup>6+</sup>). Cr<sup>3+</sup> is a major metal in living organisms for maintaining effective lipids, glucose, and protein metabolism. On the other hand, Cr<sup>6+</sup> is a dangerous ionic species and a widespread industrial pollutant. It spreads in aquatic environments, usually via waste from chemical smelting, light industry textile, cooling tower blow down, electro-plating, leather tanning, etc. Consequently, even minor concentrations of Cr<sup>6+</sup> can cause significant health problems, including irritating mucous membranes and skin, targeting the respiratory tract, dental erosion, and renal damage. It is one of three globally designated carcinogenic metals. US Environmental Protection Agency has established guidelines for the acceptable quantity of Cr<sup>6+</sup> in drinking water to be less than 0.1 mg/mL [3,44,65,66,81].

Meanwhile, aluminum (Al<sup>3+</sup>) is a non-essential element for our body system. However, it is usually introduced into the human body due to different anthropogenic activities. Drinking water that is significant in aluminum concentration may become extremely hazardous. Al<sup>3+</sup> ion is thought to have an essential role in various health issues such as encephalopathy, glucose intolerance, amyotrophic lateral sclerosis, osteoporosis, Alzheimer's disease, cardiac arrest, renal failure, Parkinson's disease, and so on [19,32,67,9].

Toxic metal ions such as Mn<sup>7+</sup>, Cr<sup>6+</sup> and Al<sup>3+</sup> can be detected in contaminated aquatic ecosystems using numerous conventional approaches such as UV-vis spectrometry, chromatography, electrochemical techniques and fluorescent sensors. However, sample preparation is difficult and time-consuming in most of these techniques. Compared to other conventional methods employed for detecting hazardous contaminants, detection by fluorescence is regarded most effective due to its high sensitivity and low cost. Several recent researches on fluorescence detection have been performed based on fluorescent molecularly imprinted polymers, metal-organic frameworks such as cationic Metal-organic framework bearing N-heterocyclic AIE molecules, wood sponges, and other materials [31,5,6,57,60,78].

Further, the avoidance of nuclear waste discharge into the environment and the appropriate disposal of it have become significant concerns. Iodine radioisotopes (<sup>129</sup>I & <sup>131</sup>I) are nuclear fuel's most dangerous volatile products. Owing to its extended radioactive half-life

of  $1.57 \times 10^7$  y, <sup>129</sup>I is regarded as more potent [30]. There are several viable iodine removal strategies, mainly wet distillation, electrochemical method or adsorption by activated carbon, nanocomposite membranes or nanofibers, functional materials, ionic liquids, and some other novel materials or methods. Among the approaches presented, adsorption technology is considered low-cost, eco-friendly, easy to operate, and highly efficient [17,22,33,34,37,49,50,51,52,10]. To overcome these challenges, novel hybrid nanocomposites have been developed, which could effectively help remove and detect water pollutants. Therefore, adsorbents have become advanced materials for effective iodine capture. The sorption materials include zeolites, activated carbon, porous polymer, covalent organic frameworks, metal-organic frameworks, bismuth-modified all-silica beta zeolite, bismuth and silver functionalized nickel foam composites and the millimeter-scale pitch-based hyper-cross-linked porous polymers@polyethersulfone and fluoride modified bismuth sulfide supported NaY zeolite material, Keggin-type polycationic AlO<sub>4</sub>Al<sub>12</sub>(OH)<sub>24</sub>(H<sub>2</sub>O)<sub>12</sub> intercalated MoO<sub>3</sub> composites and the two-dimensional assembly made up of ZIF-8 particles [14,28,63,64,69,70]. Developing new innovative technologies and nanomaterials necessary to remove and detect water pollutants. Polyaniline (PANI) is a conjugated polymer attributed to its easy fabrication methods, low cost, remarkable chemical and environmental stability, easily adjustable, good electrical conductivity, non-toxicity, and outstanding capacitive characteristics [73,76]. Correspondingly, LDHs are two-dimensional lamellar materials of positive layers separated by interlayer spaces constituted of water molecules and charge-compensating anions. The general LDH formula is expressed as [M<sup>II</sup><sub>1-x</sub> M<sup>III</sup><sub>x</sub> (OH)<sub>2</sub>]<sub>(A<sup>n-</sup>)<sub>x/n</sub></sub> mH<sub>2</sub>O, where M<sup>II</sup> and M<sup>III</sup> are metal cations (M<sup>II</sup> = Mg<sup>2+</sup>, Ni<sup>2+</sup>, etc. M<sup>III</sup> = Al<sup>3+</sup>, Fe<sup>3+</sup>, and other cations) and A<sup>n-</sup> are interlayer anions that may be replaced (A<sup>m-</sup> = SO<sub>4</sub><sup>2-</sup>, CO<sub>3</sub><sup>2-</sup>, Cl<sup>-</sup> and other anions). LDHs have numerous advantages, including excellent stability, nontoxicity, anion exchange properties, low cost, and simple synthesis methods [41,59,71]. Moreover, the modification of pristine LDHs in different ways (preparation methods, doping, and use of various reducing agents) results in enhanced adsorption properties such as ZIF-67/Cu-Bi-CO<sub>3</sub>-LDH and Cu/Cu<sub>2</sub>O-LDH show high adsorption efficiency for I<sub>2</sub> from aqueous solutions compared to pristine Cu-Bi-CO<sub>3</sub>-LDH and Cu-Mg-Al/LDH, respectively [16,77].

Besides, CNTs constitute one of the most significant nanomaterials owing to their distinct and different properties like excellent electrical conductivity, a large surface area, stability under harsh conditions, novel hollow-tube structures, etc. CNTs may be oxidized, resulting in the formation of CO<sub>2</sub>H groups on their surfaces [41,73]. Likewise, the PANI contains high numbers of imine and amine functional groups. The primary characteristic of each phase in hybrid structures can be preserved or even improved by incorporating choice functional inorganic layered materials and organic moieties via self-assembly, intercalation, or grafting, and the interaction of notably different components leads to novel properties. Thus, it is envisaged that the organic PANI will be modified onto the inorganic LDHs and organic CNTs to create the hybrid material of PANI/LDH@CNT by in-situ oxidative polymerization [82]. In this work, the layers of Pr-Co/LDH affect the iodine adsorption process, especially by adding rare earth minerals, and it was reinforced by adding PANI and CNT to increase the number of electronic transitions. PANI/LDH@CNT nanocomposite that inherits the properties of PANI, Pr-Co/LDH, and CNT materials can be tested as sensors against Mn<sup>7+</sup>, Cr<sup>6+</sup> and Al<sup>3+</sup> ions. Moreover, it is used as an adsorbent to capture dangerous chemicals such as iodine.

## 2. Experimental

### 2.1. Materials

Carbonnanotubes [CNTs], potassium persulfate ( $K_2S_2O_8$ ), aniline [ $C_6H_7N$ ], urea [ $CO(NH_2)_2$ ], Praseodymium(III) nitrate hexahydrate [ $Pr(NO_3)_3 \cdot 6H_2O$ ], Cobalt(II) nitrate hexahydrate [ $Co(NO)_2 \cdot 6H_2O$ ], and other metal salts of nitrates were provided from Sigma-Aldrich. All the chemicals were utilized without additional purification.

### 2.2. Carboxyl group functionalized CNTs

The CNTs were treated ultrasonically using 6 mol  $L^{-1}$  of  $HNO_3$  for 20 min for the formation of the  $CO_2H$  group onto the surface of the CNTs. A magnetic stirrer vigorously shook the CNTs suspension at  $60 \pm 2^\circ C$  till dry. After cooling at  $30 \pm 2^\circ C$ , the black solid was rinsed with deionized water (DIW) till neutral, then dried at  $50 \pm 2^\circ C$  overnight in the oven.

### 2.3. Synthesis of Pr-Co/LDH

A simple hydrothermal approach was used to synthesis Pr-Co/LDH. Briefly, We added the mixed salt solution containing, [ $Co(NO_3)_2 \cdot 6H_2O$ ] (1 mmol, 0.291 g), [ $Pr(NO_3)_3 \cdot 6H_2O$ ] (0.5 mmol, 0.2175 g) and [ $CO(NH_2)_2$ ] (5 mmol, 0.3003 g) to 40 mL of DIW under continuous stirring for 10 min, gradually increase the amount of the solution to 70 mL at  $60 \pm 2^\circ C$  for 2 h. The resulting suspension was put in an autoclave at  $150 \pm 2^\circ C$  for 24 h. After the heating process, the autoclave was left to cool naturally. The solid was treated by DIW and dried at  $50 \pm 2^\circ C$  for approximately 24 h [23].

### 2.4. Synthesis of PANI/LDH

Ex-situ oxidative polymerization was used to synthesize PANI/LDH. Typically, 0.3 g of pristine Pr-Co/LDH were scattered in 100 mL methanol with stirring for 30 min, and then 1.5 mL  $C_6H_7N$  was added with continuous stirring for another 20 min. 5.55 g  $K_2S_2O_8$  was dissolved in 33 mL of 1.0 mol  $L^{-1}$  HCl solution to make  $K_2S_2O_8$  solution. After that,  $K_2S_2O_8$  solution was poured into the reaction vessel with stirring for 10 min to start the polymerization process. An ice bath kept the reaction temperature at 5–8 °C. Following the completion of the reaction, the resultant product was centrifuged, washed to remove any residual acid, and dried overnight at 80 °C. PANI was synthesized for the comparison test using the abovementioned process without the Pr-Co/LDH [40].

### 2.5. Synthesis of PANI/LDH@CNT

Pr-Co/LDH precursors are combined with the functionalized carbon nanotubes (F-CNT) powder at  $60 \pm 2^\circ C$  with stirring for 4 h before being placed in the autoclave at  $150 \pm 2^\circ C$  for 24 h. The finished product was rinsed multiple times with acetone to eliminate unreacted

species before being treated with DIW till it became neutral. The Pr-Co/LDH@CNT was placed in the oven at  $50 \pm 2^\circ C$  for 24 h. The finished product was synthesized using PANI/LDH polymerization method; only 0.3 g Pr-Co/LDH @CNT particles were employed (Scheme 1).

### 2.6. Iodine Capture

Gravimetric measurements were used to evaluate the iodine vapor uptake capacities of Pr-Co/LDH, PANI/LDH, and PANI/LDH@CNT. An open small glass vial holding 10 mg of the sample powder was put into a big glass vial containing iodine. The glass vial was heated at  $70 \pm 2^\circ C$  for a certain period. The vessel was left to cool naturally after specified time intervals. Then the vial was taken out and weighed. According to the equation below was calculated the adsorption capacity of  $I_2$  ( $q$  (mg  $g^{-1}$ )):

$$(w_2 - w_1)/w_1 \times 100 \text{ wt\%} \quad (1)$$

Where  $w_1$  and  $w_2$  are the weights of the materials before and after  $I_2$  adsorption. Moreover, the  $I_2$  capture in solution was studied by Pr-Co/LDH, PANI/LDH, and PANI/LDH@CNT. The  $I_2$ / hexane solution (100 mg  $L^{-1}$ ) was obtained by dissolving a particular amount of  $I_2$  in hexane. 10 mg of the sample was poured into 20 mL of  $I_2$  solution, stirring the mixture for some time. Following adsorption, the particles of the materials were extracted from the solution using centrifugation, and then absorbance was measured at various time intervals with a UV-visible spectrometer. The amount of iodine adsorbed at equilibrium,  $q_e$  was evaluated as follows:

$$q_e = (C_0 - C_e) \frac{V}{w} \quad (2)$$

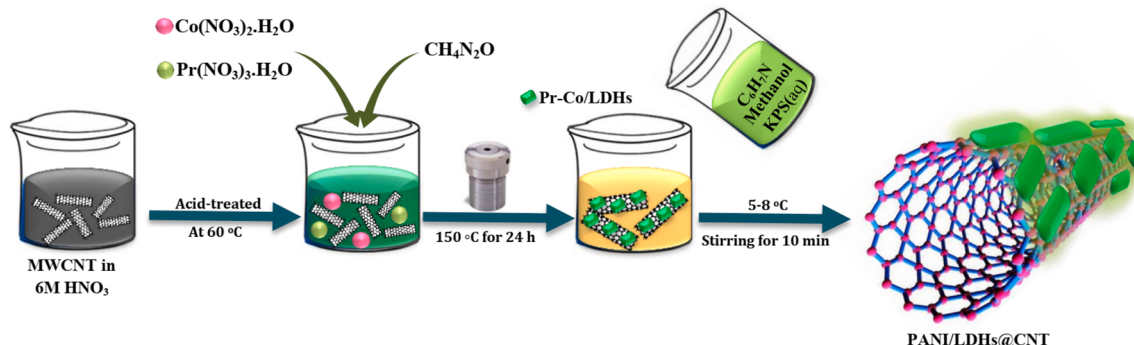
Where  $w$  is the sample weight,  $v$  is symbolized the  $I_2$  solution volume,  $C_0$  and  $C_e$  represent the iodine solution initial and ultimate concentrations (mg  $L^{-1}$ ) consecutively.

### 2.7. Release of iodine from PANI/LDH@CNT

Iodine released in ethanol was performed as follows: 10 mg of iodine-loaded PANI/LDH@CNT powder was added to 10 mL of ethanol and kept for a while. After thoroughly stirring, 0.065 mL of supernatant was extracted, diluted to 2 mL by ethanol, and analyzed by UV-Vis spectrometer at the wavelength (250–600 nm).

### 2.8. Characterization

The surface functional groups in the samples were characterized by Fourier transform infrared spectroscopy (FT-IR) using KBr discs. The crystalline nature of the materials was characterized by X-ray diffraction (XRD, Shimadzu 6100) in the range of 05–70 (2θ) by Cu Ka radiation (1.54 nm). The as-prepared nanomaterials' morphologies were



**Scheme 1.** Schematic description of PANI/LDH@CNT synthesis.

investigated by SEM coupled with an EDS system (JSM-6510LV, JOEL Japan). TEM examination of PANI/LDH@CNT was performed on (JEOL JEM2100). TGA/DTA data of the materials were studied by a Shimadzu DTG-60 H instrument in a nitrogen environment at a heating rate of 5 °C/min. The FL spectra were obtained using a Hitachi spectrofluorimeter (F-2700). Perkin Elmer Lambda-25 UV-VIS spectrometer recorded the absorbance values of each material in the wavelength region of 200–800 nm.

### 3. Results and discussion

#### 3.1. XRD analysis

The powder XRD patterns of the PAIN, F-CNT, Pr-Co/LDH, PANI/LDH, and PANI/LDH@CNT were elucidated in Fig. 1a. The F-CNT showed a strong peak at 26.0° matched to (002) plane of graphite [18, 36]. For the Pr-Co/LDH, eleven diffraction peaks at positions 13.1°, 17.9°, 23.9°, 24.9°, 26.1°, 30.5°, 32.7°, 42.4°, 44.6°, 46.9°, 52.4°, and 57.1°. The XRD pattern of Pr-Co/LDH matches well with the standard models of  $\text{Pr}_2\text{O}_3$  (JCPDS No. 82-1401),  $\text{Pr}(\text{OH})_3$  (JCPDS No. 83-2304),  $\text{Co}(\text{OH})_2$  (JCPDS No. 45-0031) and  $\text{CoO}$  (JCPDS No. 75-0533). This compatibility may indicate the purity of the material, and one of the indicators that may be taken into account is the preparation of the material in a safe environment, where water was the reaction medium. The disappearance of most of the virgin Pr-Co/LDH in the PANI/LDH might be caused by the PANI coating of the Pr-Co/LDH surface in the polymerization process. There is a noticeable difference in the crystalline property of PANI/LDH and PANI/LDH@CNT, whereby F-CNT improves the crystallinity of the PANI/LDH@CNT considerably. Many studies have introduced nano fillers to prepare nanocomposites to improve some properties of polymers such as enhancing crystallinity. Among these nano fillers are carbon nanotubes (CNTs), which can significantly improve the crystallization ability of polymers with only a small amount of addition [58]. The PANI/LDH@CNT nanocomposite shows peaks corresponding to PAIN at 26.2°, 27.3°, 28.5°, 29.5°, 44.8° as well as a peak at 46.8° corresponding to the (0 2 0), (0 1 1), and (2 0 0) crystal planes of PAIN, respectively. When the F-CNT was coated and interwoven with PANI, the XRD peak of the F-CNT at (26.0°) overlapped with the peak of the PANI at (26.1°), which resulted in a sharp and strong peak in the PANI/LDH@CNT. Some of the reflections in the PANI/LDH@CNT were consistent with those in virgin Pr-Co/LDH, specifically at 23.9°, 26.1°, 30.5°, 42.4°, 46.9°, and 52.4°. These results confirm that the virgin Pr-Co/LDH has grown and interwoven successfully with F-CNT and PANI. At the same time, the F-CNT was well dispersed in the polymer matrix, which is also evident from SEM.

#### 3.2. FT-IR spectral analysis

Typically FT-IR spectrum of the Pr-Co/LDH, PANI/LDH, and PANI/LDH@CNT nanocomposite between 4000 and 400  $\text{cm}^{-1}$  are depicted in Fig. 1b. In all the samples, a peak was generated by stretching vibration of  $\text{H}_2\text{O}$  molecules within the range of 3200–3600  $\text{cm}^{-1}$  [3]. The FT-IR spectra of PANI/LDH and PANI/LDH@CNT differ from that of bare Pr-Co/LDH. The magnified FT-IR spectrums of PANI/LDH and PANI/LDH@CNT are presented in Fig. S1. The bands at 1150, and 1298  $\text{cm}^{-1}$  of PANI/LDH and PANI/LDH@CNT are the C-N stretching bands of an aromatic amine [82], while the bands at 1487, and 1573  $\text{cm}^{-1}$  ascribed to C=C stretching vibration of rings [3]. In Pr-Co/LDH, the band at 1384  $\text{cm}^{-1}$  indicated the stretching vibration of nitrate anion ( $\text{NO}_3^-$ ). The decay of this band in PANI/LDH and PANI/LDH@CNT demonstrates that during the polymerization process, PANI was intercalated into the interfacial space of Pr-Co/LDH and ( $\text{NO}_3^-$ ) removed [72]. Lastly, the bands under 1000  $\text{cm}^{-1}$  are ascribed to the metal and oxygen lattice vibrations credited to (M-OH, M-O, and M-O-M) in hydrotalcite-like lattice [40, 47, 68, 80]. The above FTIR results demonstrate the existence of PANI, Pr-Co/LDH, and F-CNT components, indicating F-CNT's successful modification of PANI and Pr-Co/LDH.

#### 3.3. SEM and TEM analysis

The surface morphology of the pristine Pr-Co/LDH, PANI/LDH, and PANI/LDH@CNT nanocomposite was examined by SEM and TEM techniques, and the results are depicted in Fig. 2. As revealed in Fig. 2a & b, the pristine Pr-Co/LDH owns a sheet structure with a nanoscale thickness. Fig. 2c presents that the sheet-like Pr-Co/LDH structures are changed to a certain degree in acidic and a PANI coated on the Pr-Co/LDH surface. Fig. 2d exhibits the flowerlike PANI that is aggregated and grown on the Pr-Co/LDH surface. Fig. 2e & f prove that when the F-CNT was added, the sheet of the Pr-Co/LDH was rearranged so that they became more evident. After the oxidative chemical polymerization of aniline, LDH was entirely covered by the PANI, forming the core-shell structure of the nanocomposite. The surface of the PANI/LDH@CNT nanocomposite was very smooth, and the diameter was 0.5–2  $\mu\text{m}$ . On the other hand, in some sites appear PANI and F-CNT intertwined as straws or bristles on the surface of the sheets of the Pr-Co/LDH.

The TEM images of the PANI/LDH@CNT nanocomposite under different magnifications are illustrated in Fig. 2. Pr-Co/LDH present on the surface of F-CNT is described in Fig. 2g-i. In some places of Fig. 2i, Pr-Co/LDH sheets had a Grid-like shape, and these Grids were located between F-CNT cylinders. Notably, the surfaces of the F-CNT and Pr-Co/LDH in the PANI/LDH@CNT nanocomposite were covered with PANI layers. As depicted in Fig. 3b, the EDS spectra confirmed the presence of C, O, S, N, Co, and Pr elements in the PANI/LDH@CNT nanocomposite,

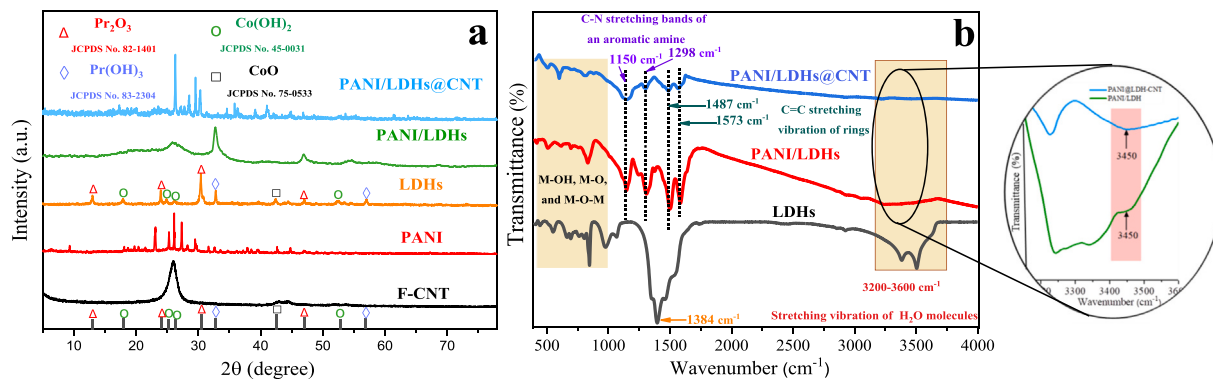


**Fig. 1.** (a) XRD patterns of the PANI, F-CNT, Pr-Co/LDH, PANI/LDH, and PANI/LDH@CNT nanocomposite. (b) FTIR patterns of Pr-Co/LDH, PANI/LDHs, and PANI/LDH@CNT, and magnified FTIR spectra of PANI/LDH and PANI/LDH@CNT nanocomposite.

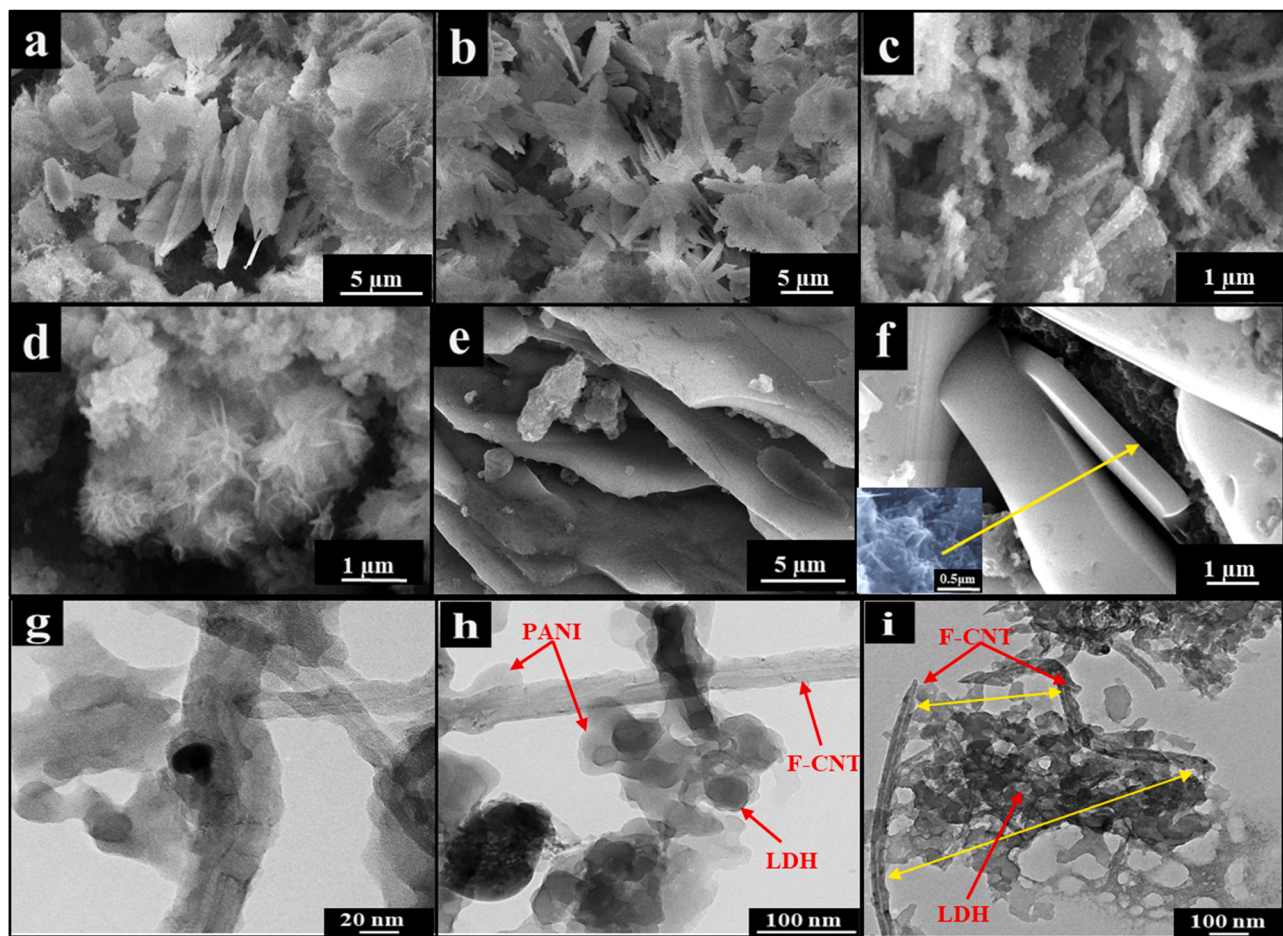


**Fig. 2.** SEM images of (a & b) pristine Pr-Co/LDH, (c & d) PANI/LDH, and (e & f) PANI/LDH@CNT; The inset in (f) shows high-magnification of respective SEM images. TEM images of (g-i) PANI/LDH@CNT.

indicating the existence of the Pr-Co/LDH, F-CNT, and PANI. In the same context, Fig. 3a shows that the previous elements are well dispersed on PANI/LDH@CNT nanocomposite surface.

#### 3.4. TGA-DTA analysis

The thermal behavior of the raw Pr-Co/LDH, PANI/LDH, and PANI/LDH@CNT can be recognized by thermogravimetric analysis, as illustrated in Fig. 4. Decomposition of raw Pr-Co/LDH occurs in three thermal degradation stages. The TGA/DTA curve of raw Pr-Co/LDH is shown in Fig. 4a. The initial step in the range of 30–246.3 °C (5.1 %) is owing to the removal of water molecules from the surface of Pr-Co/LDH [42], which can be corroborated by the exothermic peaks obtained at 239.8 °C. The second mass loss (10.2 %) at temperatures ranging from 246.3 to 434.8 °C is related to dehydroxylation and denitration [11,13], which corresponds to an exothermic peak at 360.6 °C. The last mass loss (14.4 %) observed above 434.8 °C was probably attributed to continuous dehydroxylation [28] with an endothermic peak at 467.3 °C. On the other hand, the TGA curve of PANI/LDH contained two central descent stages as shown in Fig. 4b. The first step from 44.6 to about 202.2 °C (5.04 %) is ascribed to the loss of interlayer and physically adsorbed water. The significant weight loss of the PANI/LDH starts beyond 202.2 °C (85.6 %), results from the dehydroxylation of the Pr-Co/LDH layer, the loss of acid dopant (HCl), the degradation of PANI in the hybrid composite and decomposition of polymer backbone chain [14,82]. The DTA curve of PANI/LDH showed two peaks, one endothermic at 79.36 °C and the other exothermic at 500.8 °C. In contrast, the slow weight loss (6.3 %) was observed for PANI/LDH@CNT

nanocomposite up to 348 °C as shown in Fig. 4c, indicating the removal of physically adsorbed water molecules. The decomposition of the PANI/LDH@CNT occurs in temperature regions ranging from 348 to 550 °C (33.1 %) assigned to the decomposition of polymer chains, dehydroxylation, the release of co-intercalated HCl and production metal oxides, and between 550 to approximately 800 °C (12.5 %) corresponding to the degradation of PANI in the nanocomposite [61]. The remaining weight loss was attributed to the functional groups of the acid-treated CNTs [12]. The DTA analysis of the PANI/LDH@CNT nanocomposite (Fig. 4c) shows exothermic peaks at 495.5 and 5514.7 °C, as well as an exothermic peak at 76.6 °C. The total mass loss for PANI/LDH@CNT was (51.9 %), which was lower than PANI/LDH (90.64 %). Therefore, F-CNT can enhance the thermal stability of PANI/LDH@CNT compared with PANI/LDH.

#### 3.5. Iodine adsorption

Due to the existence of free amine (-N) groups in PANI, OH<sup>-</sup> of Pr-Co/LDH and CO<sub>2</sub>H, and the π-electron-rich in F-CNT. Therefore, it was expected that the designed PANI/LDH@CNT would be an excellent option for the adsorption of iodine. In order to investigate I<sub>2</sub> capture capability, the PANI/LDH@CNT powder was subjected to I<sub>2</sub> vapor in an isolated system at 343 K, and I<sub>2</sub> adsorption was evaluated at various time periods, as depicted in Fig. 5a & b. The results show that I<sub>2</sub> adsorption gradually rose throughout the first 9, 19, and 25 h for CNT, PANI, Pr-Co/LDH, PANI/LDH, and PANI/LDH@CNT, respectively. At the same time, no extra change was recorded, indicating that the system was saturated. The iodine adsorption capacity for PANI/LDH@CNT in

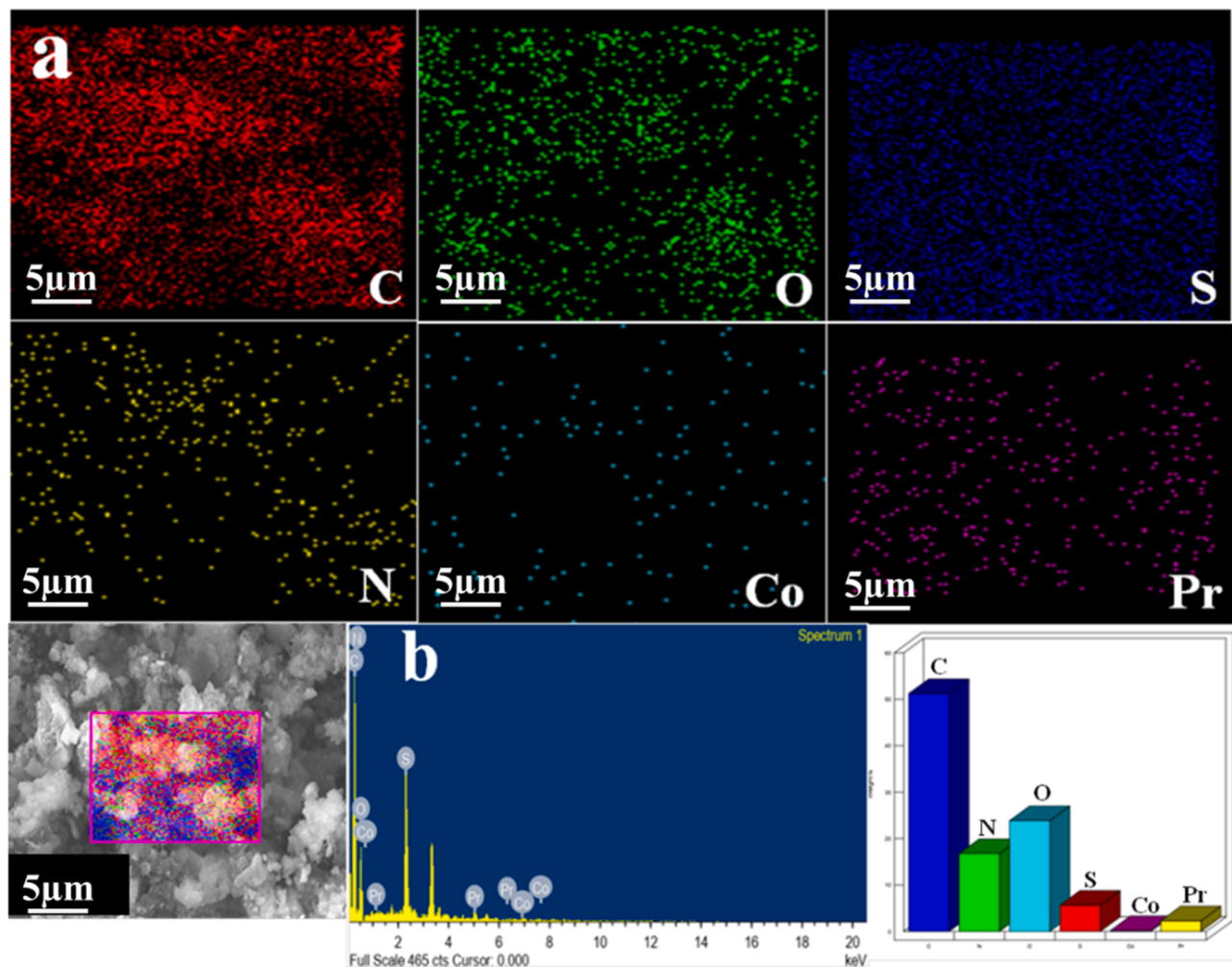


**Fig. 3.** (a) EDS mappings (C, O, S, N, Co, and Pr) of PANI/LDH@CNT (b) EDS morphological diagram of PANI/LDH@CNT nanocomposite.

the vapor phase was about 900 mg g<sup>-1</sup>, through gravimetric calculation, which is relatively 3 times greater than the liquid phase. Compared with some solid porous adsorbents, the removal efficiency of PANI/LDH@CNT for iodine is pretty high, as shown in Table S1.

In addition, Pr-Co/LDH, PANI/LDH, and PANI/LDH@CNT can also be employed as iodine absorbents in organic solutions. For the adsorption capacity, 10 mg of the PANI/LDH@CNT was immersed in 20 mL of different iodine concentrations in hexane (100, 150, 200, and 250 mg L<sup>-1</sup>) in a small closed vial for 9 h at room temperature (RT). The maximum adsorption capacity and removal percentage of PANI/LDH@CNT are illustrated in Fig. 6a & b, respectively. With the rise of the I<sub>2</sub> concentration in hexane, the adsorption capacity increased until the maximum adsorption capacity was attained. The highest adsorption capacity in 250 mg L<sup>-1</sup> of the solution was 303.20 mg g<sup>-1</sup>. Fig. 6c depicts the color change of several I<sub>2</sub> solutions in hexane before and after PANI/LDH@CNT uptake.

The concentration of remaining I<sub>2</sub> was estimated using UV-vis spectroscopy, as demonstrated in Fig. 7a, b, & Fig. S2, where the best removal efficiency was reported to be up to 97.11 % for an iodine solution of 100 mg L<sup>-1</sup>, approximately all of the I<sub>2</sub> was eliminated from the hexane solution. While comparing, the lowest iodine removal efficiency reached 60.4 % for an I<sub>2</sub> solution of 250 mg L<sup>-1</sup>, suggesting that adsorption of PANI/LDH@CNTs might be a promising option for practical application. A comparison of adsorption capabilities with several well-known adsorbents was undertaken, and the results are reported in Table S1.

### 3.5.1. Adsorption kinetics

To describe the adsorption behavior of PANI/LDH@CNT, two standard theoretical models were studied. The studied adsorption kinetic models are the PFO (Eq.3) and PSO (Eq.4):

$$\log(q_e - q_t) = \log q_e - \left( \frac{k_1}{2.303t} \right) \quad (3)$$

$$\frac{t}{q_t} = \left( \frac{1}{k_2 q_e^2} \right) + \left( \frac{t}{q_e} \right) \quad (4)$$

Where q<sub>e</sub> (mg g<sup>-1</sup>) is the adsorption capacity of I<sub>2</sub> at equilibrium, while q<sub>t</sub> (mg g<sup>-1</sup>) is the adsorption capacity at a particular time t (min), k<sub>1</sub> (min<sup>-1</sup>) and k<sub>2</sub> (g mg<sup>-1</sup> min<sup>-1</sup>) are the rate constants of PFO and PSO, respectively. As shown in Table 1, the R<sup>2</sup> value of the PFO is 0.990, which is closer to 1.0 than that of the PSO (0.989). Therefore, the adsorption kinetic data can be well described by the PFO (Fig. S3). As the adsorption time progresses, the contact reaction gradually reaches equilibrium. After 9 h of reaction, the removal rates of CNT, PANI, Pr-Co/LDH, LDH/PANI, and LDH/PANI@CNT were 14.68 %, 12.15 %, 16.42 %, 61.62 % and 97.11 %, respectively (Fig. S4). Therefore, LDH/PANI@CNT should be chosen as a model for further research.

### 3.5.2. Adsorption isotherm

To further describe the interactions between iodine and PANI/LDH@CNT, isotherm studies were conducted, as shown in Fig. S5 a & b. The Freundlich and Langmuir models were used to simulate the

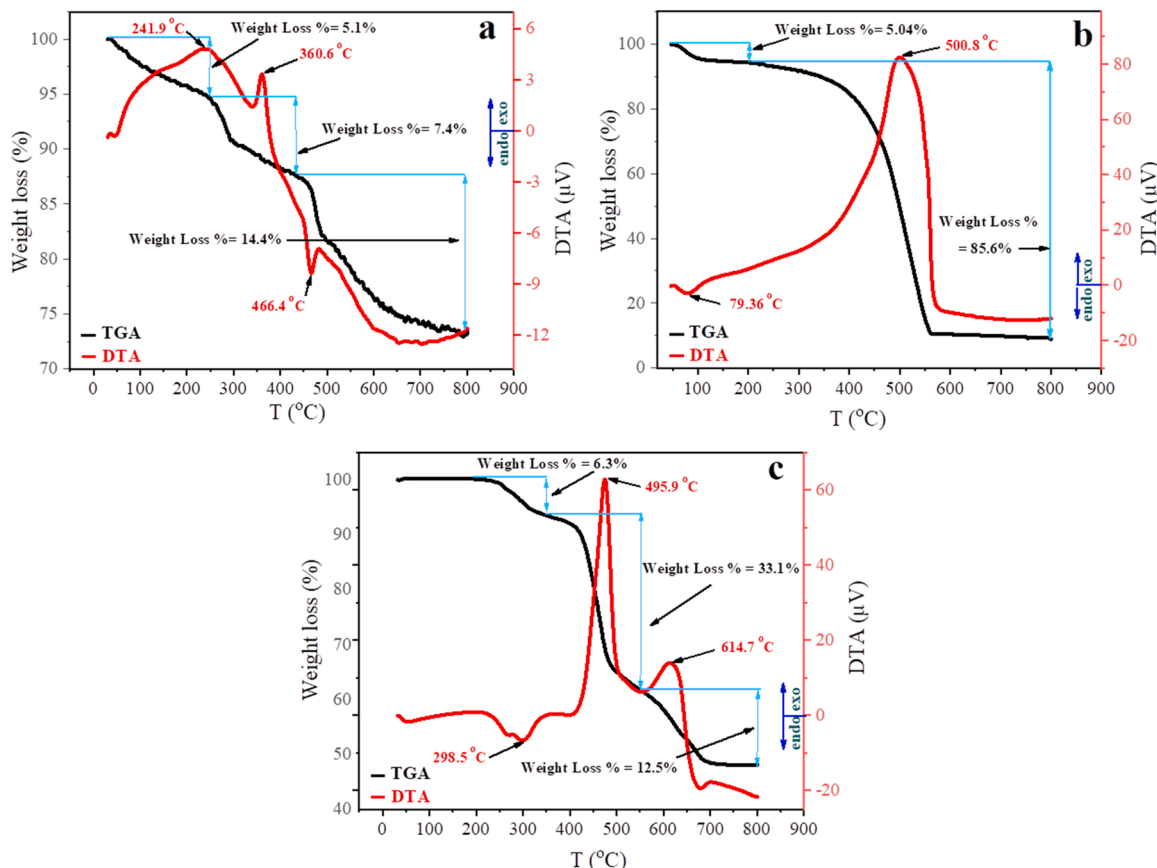


Fig. 4. TGA/DTA curves of (a) raw Pr-Co/LDH, (b) PANI/LDH, and (c) PANI/LDH@CNT nanocomposite.

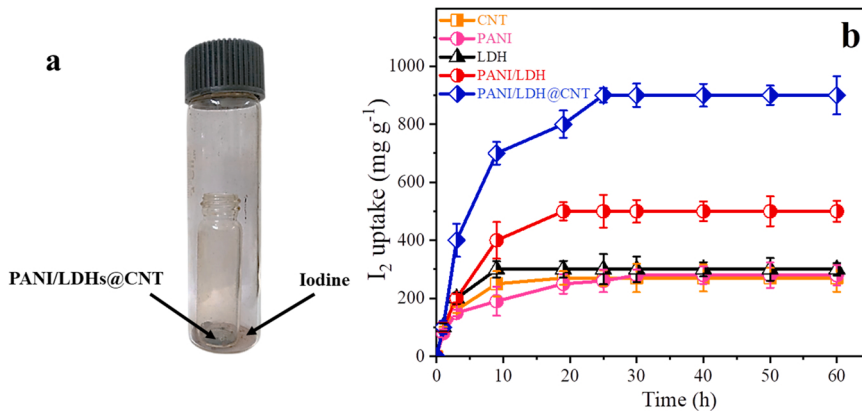


Fig. 5. (a) Photographic illustration of the iodine capture method by Gravimetric measurements, (b) gravimetric changes of iodine adsorption capacity of F-CNT, PANI Pr-Co/LDH, PANI/LDH, and PANI/LDH@CNT as a function of time at 343 K.

adsorption behavior of iodine ( $100\text{--}250\text{ mg L}^{-1}$ ) onto the PANI/LDH@CNT in Eqs. (5), and (6) respectively [56]:

$$\log q_e = \log K_f + \left( \frac{1}{n} \log C_e \right) \quad (5)$$

Where  $q_e$  is the adsorbed amount ( $\text{mg g}^{-1}$ ),  $C_e$  is the concentration at equilibrium, and  $K_f$  and  $n_f$  are Freundlich constants.

$$\frac{C_e}{q_e} = \left( \frac{1}{K_L q_m} \right) + \left( \frac{C_e}{q_m} \right) \quad (6)$$

Where  $q_e$  is adsorbed  $I_2$  at equilibrium ( $\text{mg g}^{-1}$ ), where  $C_e$  is the rest

concentration ( $\text{mg L}^{-1}$ ),  $q_m$  is the maximum coverage capacity of the monolayer ( $\text{mg g}^{-1}$ ), and  $K_L$  is the Langmuir isotherm constant ( $\text{L mg}^{-1}$ ). The results included in Table 2 indicated that the Langmuir model was the best fit for iodine adsorption ( $R^2 = 0.999$ ) founded on PANI/LDH@CNT. Moreover, it meant that iodine adsorption on PANI/LDH@CNT was monolayer adsorption and occurred on the specific homogeneous sites on the surface [59]. PANI/LDH@CNT nanocomposite exhibits excellent adsorption performance, and the maximum iodine adsorption capacity is  $309.60\text{ mg g}^{-1}$ .  $K_f$  values of  $170.9\text{ L g}^{-1}$  ( $I_2$ ) indicate a high adsorption intensity and capacity [56]. For Langmuir model, the  $K_L$  values between 0 and 1 meant that the adsorption of iodine onto PANI/LDH@CNT was an excellent process [53].

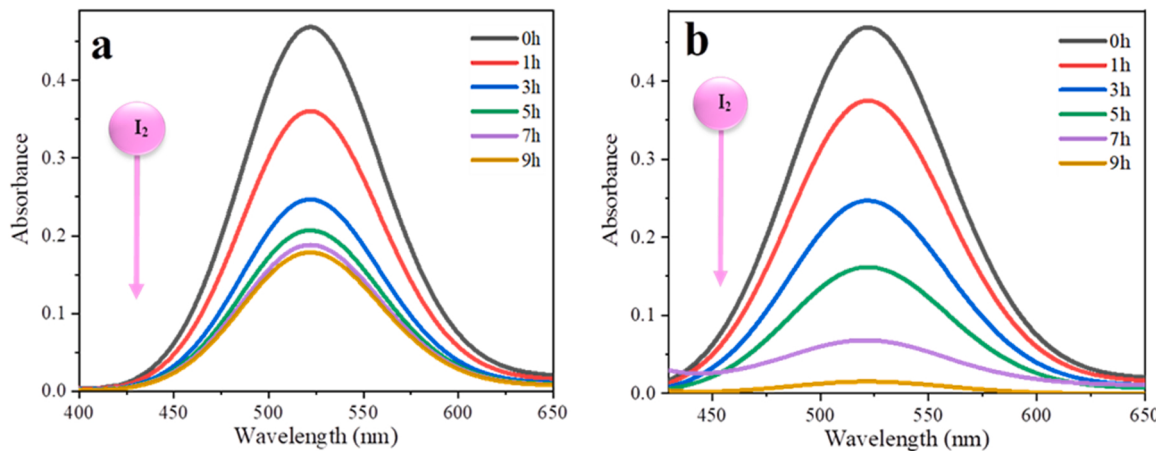
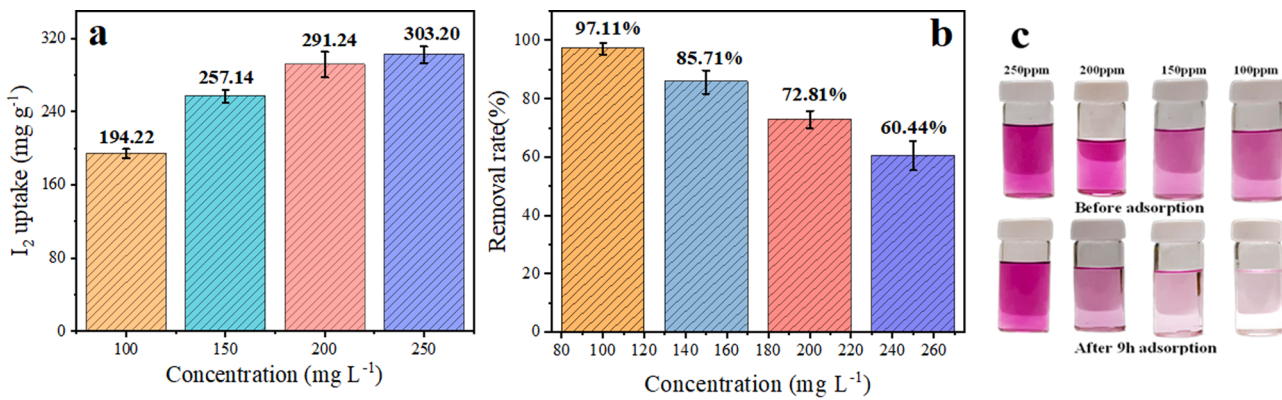


**Table 1**  
Kinetic parameters for  $I_2$  removal by Pr-Co/LDH, PANI/LDH, and PANI/LDH@CNT.

Adsorbent	$q_e$ (exp) ( $\text{mg g}^{-1}$ )	Pseudo-first order			Pseudo-second order		
		$q_e$ (cal) ( $\text{mg g}^{-1}$ )	$k_1$ ( $\text{min}^{-1}$ )	$R^2$	$q_e$ (cal) ( $\text{mg g}^{-1}$ )	$K_2 \times 10^{-2}$ ( $\text{g mg}^{-1} \text{ min}^{-1}$ )	$R^2$
LDH	32.80	22.40	0.28	0.991	37.98	1.50	0.989
PANI/LDH	123.84	127.56	0.49	0.998	155.04	0.31	0.996
PANI/LDH@CNT	194.22	246.55	0.34	0.990	384.62	0.03	0.989

**Table 2**  
Langmuir and Freundlich isotherm parameters for  $I_2$  removal using PANI/LDH@CNT.

Adsorbent	Adsorbate	Langmuir constants			Freundlich constants		
		$q_m$ (cal) ( $\text{mg g}^{-1}$ )	$K_L$ ( $\text{L mg}^{-1}$ )	$R^2$	$K_f$ ( $\text{L g}^{-1}$ )	$n_f$	$R^2$
PANI/LDH@CNT	$I_2$	309.60	0.893	.999	170.90	7.76	0.991

### 3.5.3. Mechanism of $I_2$ adsorption by PANI/LDH@CNT

In order to study the adsorption property relationship of the PANI/LDH@CNT and the mechanism of binding, SEM, PXRD, TGA, IR, EDS, and Raman were performed before and after iodine uptake. SEM images of PANI/LDH@CNT after adsorption of iodine are presented in Fig. 8a. The nanostructure and morphology of the composite are much more preserved, probably due to surface complexation, and strong ionic interaction between iodine and amine (-N),  $\text{CO}_2\text{H}$ ,  $\text{OH}^-$ , and the  $\pi$ -electron-rich in CNT [3]. Fig. 8b shows the TGA curve of PANI/LDH@CNT- $I_2$  along with that of the PANI/LDH@CNT for comparison.

The TGA graph of the PANI/LDH@CNT- $I_2$  exhibits a broad mass loss step from 63.3° to 560.9°C, which is attributed to the release of poly-iodides. On the other hand, we can see that PANI/LDH@CNT has higher temperature stability (stable up to 268.7 °C). The shift in the spectra, increase, decrease and disappearance of the peaks can be used to see whether there was an effect of iodine adsorption by different functional groups [48]. To determine which functional groups contributed to the adsorption of the iodine on PANI / LDH @ CNT, FT-IR study was carried out after contact with iodine, as illustrated in Fig. 8c. It was observed that before the introduction of the iodine, two peaks appeared at around

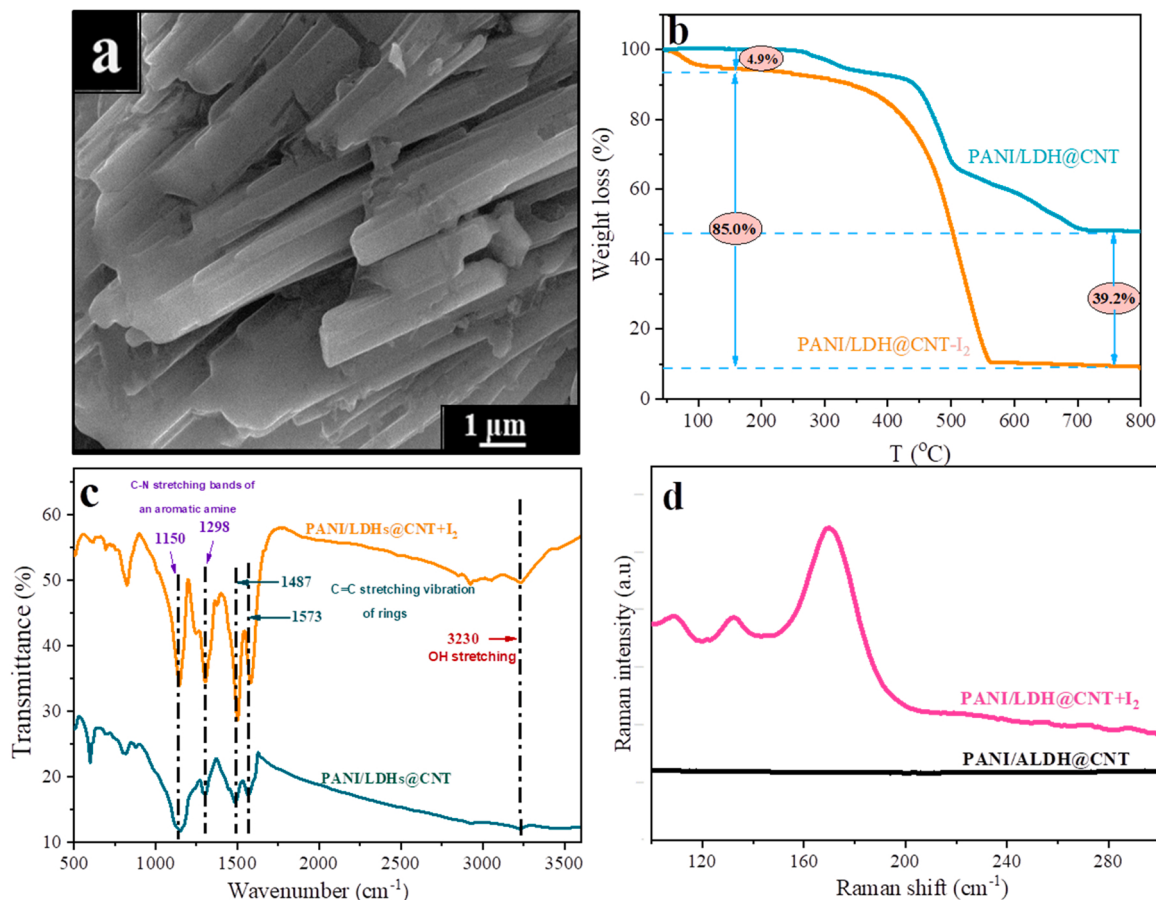


**Fig. 8.** (a) SEM image of PANI/LDH@CNT after uptake iodine (b) TGA trace under N<sub>2</sub> atmosphere of PANI/LDH@CNT and PANI/LDH@CNT+I<sub>2</sub>, (c) FTIR spectra of PANI/LDH@CNT before and after the addition of I<sub>2</sub>, and (d) Raman spectra of iodine-doped PANI/LDH@CNT in comparison to pristine PANI/LDH@CNT.

1150 and 1298 cm<sup>-1</sup> corresponding to C-N stretching bands of an aromatic amine, as well as a peak at 3230 cm<sup>-1</sup> attributed to OH<sup>-</sup> stretching, but after adsorption of iodine, there is only a difference in the intensity of adsorption, while the location of the peaks remained constant. In addition, there are two peaks that appear at 1487, and 1573 cm<sup>-1</sup> ascribed to C=C stretching vibration of rings, but after the adsorption, there is a difference in the intensity of adsorption, where the peaks became strengthened and the peak shifted to 1502 and 1587 cm<sup>-1</sup> respectively. Indications are that iodine adsorption could occur at OH<sup>-</sup> and C-N units and aromatic rings in the PANI/LDH@CNT, similar to the phenomenon observed in iodine-doped PANI [45]. This is most likely due to the formation of a charge transfer (CT) complex between PANI/LDH@CNT and polyiodide anions as indicated by a similar case of iodine-loaded porous conjugated organic cages [25].

Moreover, the existence of iodine in PANI/LDH@CNT following the adsorption study was verified using EDS spectra (Fig. S6a). The PXRD patterns of PANI/LDH@CNT and PANI/LDH@CNT-I<sub>2</sub> show that the location of the peaks shifted slightly and their intensity changed, but the characteristic absorption peaks of PANI/LDH@CNT still existed; this indicates that the sorbent retained its typical structure after the iodine adsorption (Fig. S6b).

Raman spectroscopy was used to obtain qualitative information on the nature of iodine in the PANI/LDH@CNT. The loaded PANI/LDH@CNT was characterized by a strong peak at 169 cm<sup>-1</sup>, attributed to I<sub>3</sub><sup>-</sup> anions [4]. Two other Raman peaks with medium-weak intensities at lower wave numbers, 108 cm<sup>-1</sup> and 132 cm<sup>-1</sup>, corresponding to the presence of I<sub>3</sub><sup>-</sup> anions attached to PANI/LDH@CNT (Fig. 8d) [62]. These results indicate that the adsorbed guest iodine on PANI/LDH@CNT does not exist in the form of I<sub>2</sub>. The reason for this could be that the electrons pairs of PANI/LDH@CNT polarize the adsorbed iodine molecules into an

ionic state [74] and charge transfer (CT) interactions occur between PANI/LDH@CNT and the guest iodine, causing the formation of I<sub>3</sub><sup>-</sup> and I<sub>5</sub><sup>-</sup> [26]. Due to the presence of free amine (-N) groups in PANI and OH<sup>-</sup> groups of the Pr-Co/LDH as well as CO<sub>2</sub>H and the presence of conjugated π-electron in F-CNT [24,38], which is similar to the phenomenon observed in iodine adsorption (as vapor) on hexaphenylbenzene-based conjugated microporous polymers (HCMPs) [39]. This indicates that the behavior and mechanism of iodine adsorption as a solution do not differ from the adsorption of iodine as a vapor. Therefore, several possible interactions have been suggested to which the high uptake of iodine by PANI/LDH@CNT is attributed (Fig. 9).

### 3.5.4. Iodine release and recycling of the PANI/LDH@CNT

Iodine release occurred when the I<sub>2</sub>-loaded samples were immersed in organic solvents at RT. The process of the I<sub>2</sub> release was performed by immersing I<sub>2</sub>-loaded PANI/LDH@CNT in ethanol and monitoring the concentration of iodine solution via UV-vis spectroscopy at certain time intervals under ambient conditions. The UV-vis spectra revealed two absorbance maxima at 291 and 360 nm, which were attributed to polyiodide anions (I<sub>3</sub><sup>-</sup>, I<sub>5</sub><sup>-</sup>) [39]. The absorbance of the solution rises with time, as illustrated in the curve of I<sub>2</sub> release in ethanol at various intervals (Fig. 10a). After 150 min, the absorbance no longer changes, implying equilibrium formation. As shown in Fig. 10c, the color of the solution rapidly changed from yellow to dark brown with time, which indicates that iodine had dissociated from the PANI/LDH@CNT skeleton. We hypothesize that this release behavior is controlled by host-guest interactions, which facilitate adsorbent recyclability for reuse. In this context, recyclability is a significant criterion. To investigate the recycling ability of the PANI/LDH@CNT, ethanol was employed to eliminate any excess I<sub>2</sub> on the surface of the PANI/LDH@CNT. Then,

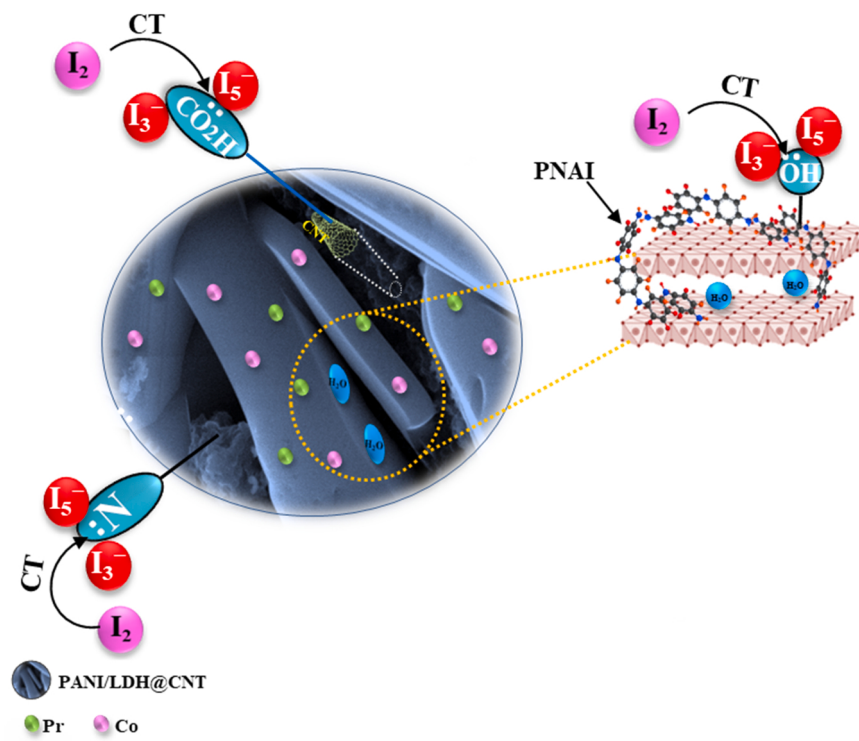


**Fig. 9.** The proposed mechanism of iodine capture by PANI/LDH@CNT.

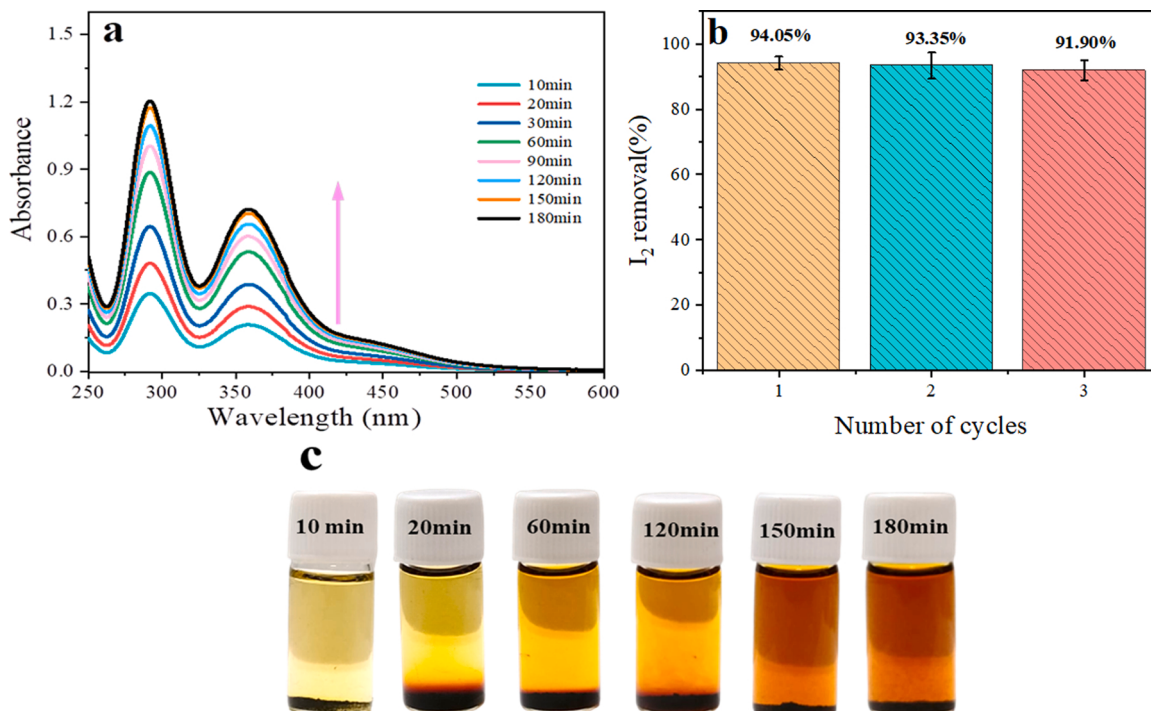


**Fig. 10.** (a) Changes in UV-Vis absorption spectra over time for the I<sub>2</sub> release from PANI/LDH@CNT in 10 mL of ethanol, (b) Recycling ability of PANI/LDH@CNT for the capture of I<sub>2</sub> from solution (recycling parameters: Initial I<sub>2</sub> concentrations= 100–250 mg L<sup>-1</sup>, V<sub>I2</sub> solution= 20 mL, adsorbent amount= 10 mg, pH= 7.0, T = 303 K, and t = 60 min), (c) Photographs showing the process of the iodine release from PANI/LDH@CNT in ethanol.

the recovered PANI/LDH@CNT was dried in an oven at 60 ± 2 °C before reusing. In Fig. 10b, the recycling ability of PANI/LDH@CNT for I<sub>2</sub> removal during three consecutive cycles. The I<sub>2</sub> recycling percentage (Rp) of recovered PANI/LDH@CNT was 94.05 % upon completion of the first cycle. After an additional two cycles, the PANI/LDH@CNT still had

a very high removal efficiency (Er) of 90.12 %, which suggests that these extremely high values make PANI/LDH@CNT a promising candidate for usage as powerful recyclable and reversible I<sub>2</sub> capture adsorbents. On the other hand, the XRD and FT-IR of the PANI/LDH@CNT after the reuse of iodine capture were performed, where Fig. S6c and Fig. S6

d showed that after the process of washing the absorbent material in order to reuse it, the peaks returned to their positions before the adsorption process, while the change in their intensity remained, but very slightly, due to iodine binding to free amine groups (-N) in PANI in addition to OH<sup>-</sup> on the layers Pr-Co/LDH as well as CO<sub>2</sub>H in F-CNT by charge transfer reaction; therefore there may be iodine residue on the adsorption material, this is demonstrated by studying the recycling capacity of the material (Fig. 10b), where we noticed that there is a slight decrease in the recycling ratio from 94.05 % to 90.12 %.

### 3.6. Fluorescence studies of PANI/LDH@CNT

#### 3.6.1. Optimization of reaction conditions

The fluorescence spectra of Pr-Co/LDH, PANI/LDH, and PANI/LDH@CNT nanocomposite are shown in Fig. S7a. The FL intensity is observed to be smallest for Pr-Co/LDH and largest for PANI/LDH@CNT nanocomposite, where it reached 1381.1, indicating that F-CNT worked to improve the nanocomposite and control its properties. The FL spectra of PANI/LDH@CNT nanocomposite show distinct excitation and emission peaks at 280 and 332 nm, as illustrated in (Fig. S7b). The FL intensity of PANI/LDH@CNT is maximum at neutral pH (7.0) while decreasing in basic as well as acidic pH (Fig. S7c). The effect of pH of Mn<sup>7+</sup> and Cr<sup>6+</sup> solutions on the FL intensity of PANI/LDH@CNT is shown in Fig. S7d & e. It is observed that the FL intensity was reduced to the maximum at neutral pH for Mn<sup>7+</sup> and Cr<sup>6+</sup> solutions.

#### 3.6.2. Fluorescence "Turn-Off" sensing of Cr<sup>6+</sup> and Mn<sup>7+</sup> ions

The fluorescent response of PANI/LDH@CNT nanocomposite to some metal ions (Pb<sup>2+</sup>, Cr<sup>3+</sup>, Cd<sup>2+</sup>, Ca<sup>2+</sup>, As<sup>5+</sup>, Cr<sup>6+</sup>, Mn<sup>7+</sup>, Zn<sup>2+</sup>, Hg<sup>2+</sup>, and Al<sup>3+</sup>) was investigated in by introducing 2 ppm aqueous solution containing various metal ions individually to 3 mg of PANI/LDH@CNT nanocomposite scattered in 10 mL of deionized water at temperature room. Fluorescence-based titration was performed through gradually adding various metal ions to the aqueous solution of PANI/LDH@CNT (Fig. 11). Fluorescence quenching was noted to moderately increase with Pb<sup>2+</sup>, Cr<sup>3+</sup>, Cd<sup>2+</sup>, Ca<sup>2+</sup>, and As<sup>5+</sup> ions, except for Zn<sup>2+</sup>, Hg<sup>2+</sup>, and Al<sup>3+</sup>, which have a high fluorescence intensity. Notably, a significant improvement in fluorescence quenching was seen when only 200 ppb of Cr<sup>6+</sup> and Mn<sup>7+</sup> ions solutions were added. These results indicate that PANI/LDH@CNT might be used as a "turn-off" fluorescent probe for detecting Cr<sup>6+</sup> as well as Mn<sup>7+</sup>, as well as a "turn-on" sensor for the detection of Al<sup>3+</sup> ion in water.

Fluorescence titration tests were performed with the stepwise addition of Cr<sup>6+</sup> and Mn<sup>7+</sup> ions from 0 to 400 ppb to explore the turn-off sensing capacity of PANI/LDH@CNT toward Cr<sup>6+</sup> and Mn<sup>7+</sup>, as shown in Fig. 12a, & b. Interestingly, fast and high fluorescence quenching was

observed upon incremental addition of Cr<sup>6+</sup> and Mn<sup>7+</sup> solution. Similarly, titration-based fluorescence studies were carried out with the remaining metal ions. PANI/LDH@CNT changes with various metal ions in the water (Fig. S8), indicating that other metal ions have a moderately to insignificant effect on fluorescence enhancement.

The LOD for PANI/LDH@CNT nanocomposite was calculated using the formula  $3\sigma/m$  (wherein  $\sigma$  symbolized the standard deviation (SD), while  $m$  represents the slope) (Fig. 13a, b & Fig. S9) [7] to be  $5.1 \times 10^{-8}$  for Mn<sup>7+</sup> and  $5.9 \times 10^{-8}$  for Cr<sup>6+</sup>, where it outperforms many previously reported detection systems (Table S2).

Meanwhile, the quenching efficiency of Cr<sup>6+</sup> and Mn<sup>7+</sup> was calculated by the Stern-Volmer (SV) equation,  $(I_0/I) = K_{SV} [Q] + 1$ , wherein  $I_0$  and  $I$  indicate the fluorescence intensity before and after the addition of the analyte. The symbol  $I$  represent the fluorescence intensity in the existence of an analyte,  $[Q]$  corresponds to a concentration of the analyte, while the Stern-Volmer constant ( $M^{-1}$ ) is represented by the symbol  $K_{SV}$  [83]. The  $K_{SV}$  values of PANI/LDH@CNT nanocomposite for Ca<sup>2+</sup>, As<sup>5+</sup>, Cd<sup>2+</sup>, Cr<sup>6+</sup>, and Mn<sup>7+</sup> ions are found to be  $7.7 \times 10^4$ ,  $1.4 \times 10^5$ ,  $1.1 \times 10^5$ ,  $4.0 \times 10^5$  and  $1.1 \times 10^6 M^{-1}$  respectively. The high  $K_{SV}$  value suggests great sensitivity of the current PANI/LDH@CNT nanocomposite towards detecting Cr<sup>6+</sup> and Mn<sup>7+</sup> in solution, and the linear fit correlation coefficient ( $R^2$ ) of 0.998 Cr<sup>6+</sup> and 0.916 Mn<sup>7+</sup> (Fig. 13c, d & Fig. S10).

Correspondingly, different metal cations influence was examined, [ $Pb^{2+}$ ,  $Cr^{3+}$ ,  $Cd^{2+}$ ,  $Ca^{2+}$ ,  $As^{5+}$ ,  $Zn^{2+}$ ,  $Hg^{2+}$ , and  $Al^{3+}$ ] to evaluate the selectivity of PANI/LDH@CNT nanocomposite for Mn<sup>7+</sup> and Cr<sup>6+</sup> detection, where the luminescent intensities of PANI/LDH@CNT suspension were assessed to determine its selectivity in the existence of the aforementioned cation mixtures with and without Mn<sup>7+</sup> or Cr<sup>6+</sup>. As demonstrated in Fig. 14 a & b, the intensities have been less influenced by other cations but reduced when Mn<sup>7+</sup> and Cr<sup>6+</sup> were introduced, which revealed that PANI/LDH@CNT nanocomposite has a remarkable selectivity for Mn<sup>7+</sup> and Cr<sup>6+</sup> when compared to other common cations found in solutions. In this research, the PANI/LDH@CNT sensor shows no significant difference in Mn<sup>7+</sup> and Cr<sup>6+</sup> intensity when these metal ions are present.

Actually, the organic media observed in the environment often contain interfering metal ions. As a result, in order to imitate environmental conditions, several typical interfering metal ions, including Pb<sup>2+</sup>, Cr<sup>3+</sup>, Cd<sup>2+</sup>, Ca<sup>2+</sup>, As<sup>5+</sup>, Cr<sup>6+</sup>, Zn<sup>2+</sup>, Hg<sup>2+</sup>, Al<sup>3+</sup>, and Mn<sup>7+</sup> ions, were used for investigating the selectivity of the PANI/LDH@CNT. In Fig. 15, the fluorescence intensity of the PANI/LDH@CNT suspension was measured and recorded. The fluorescence quenching effect of Mn<sup>7+</sup> ions on PANI/LDH@CNT did not vary significantly after adding various mixed metal ions, demonstrating that other metal ions did not hamper the detection of Mn<sup>7+</sup> ions.

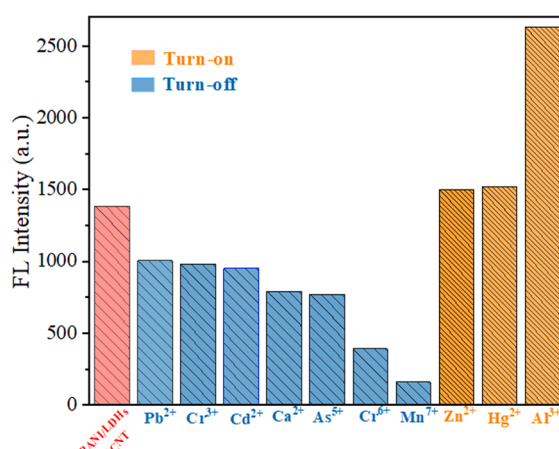
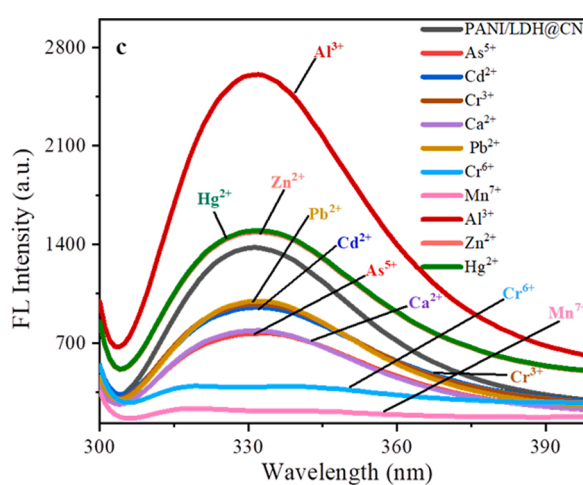


**Fig. 11.** Chang in the fluorescence spectrum of PANI/LDH@CNT nanocomposite (0.3 mg/mL) in the existence of multiple metal ions (400 ppb) in DIW (pH= 7.0).

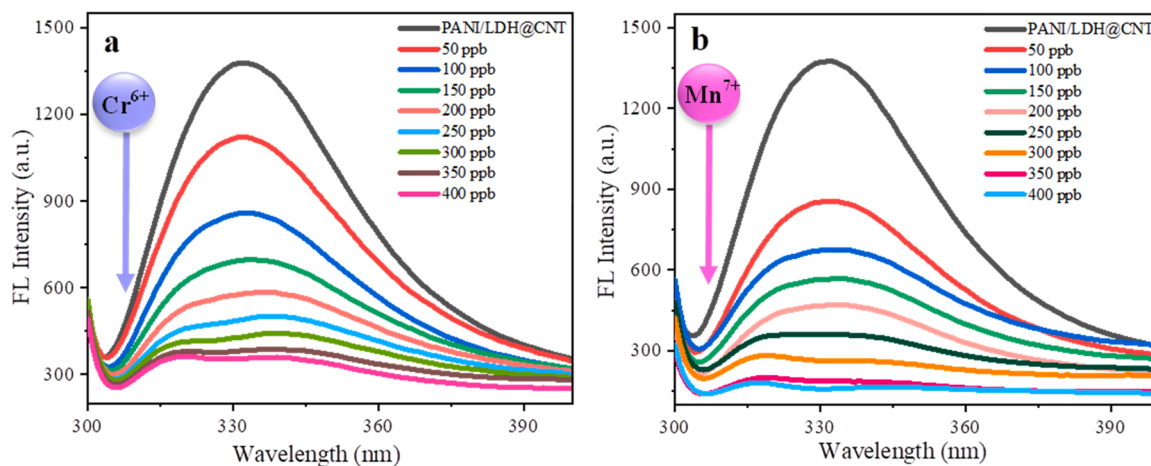


**Fig. 12.** Changes in fluorescence intensity of PANI/LDH@CNT nanocomposite ( $\lambda_{\text{ex}} = 280 \text{ nm}$ ) in deionized water (0.3 mg/mL), (pH= 7.0) at room temperature, upon incremental addition of (a) Cr<sup>6+</sup> and (b) Mn<sup>7+</sup> ions.

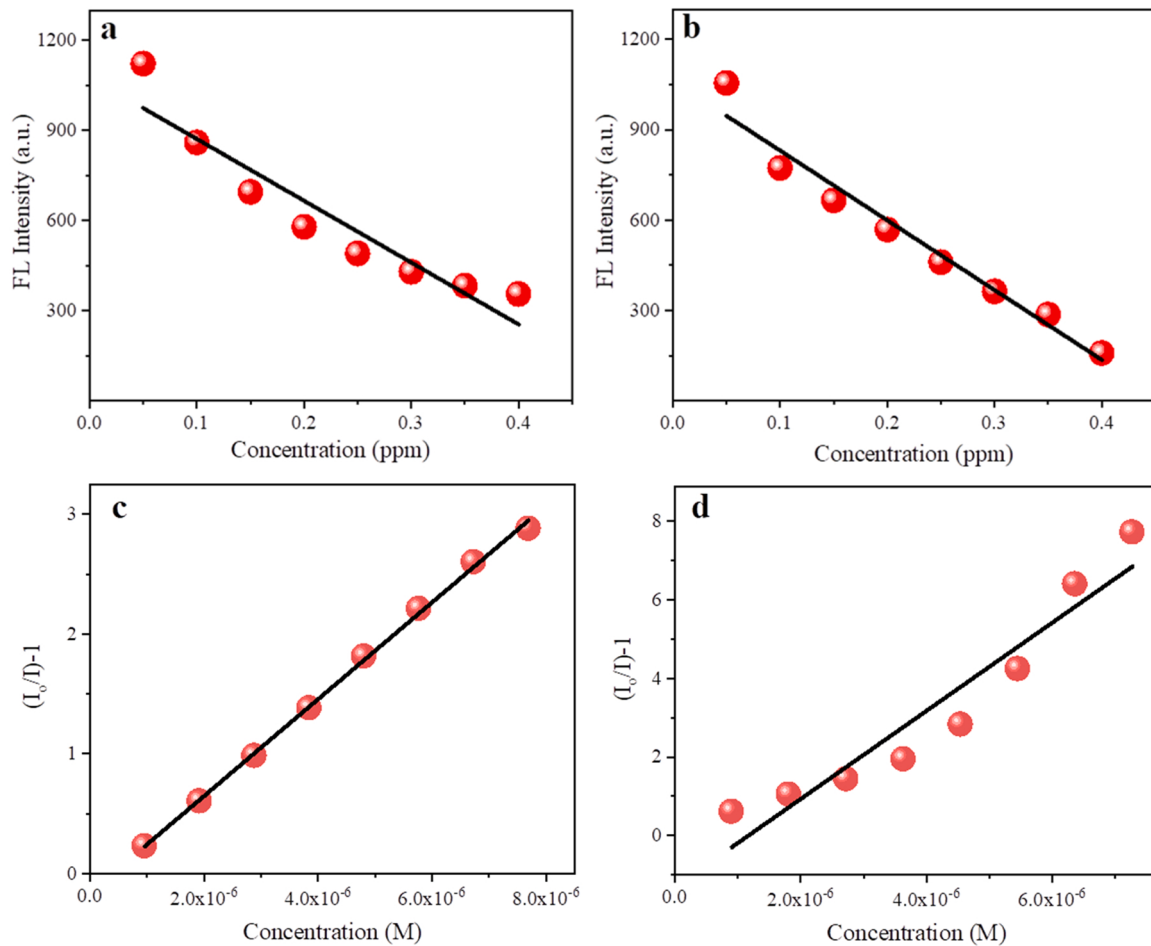


**Fig. 13.** Calculate LOD of PANI/LDH@CNT nanocomposite for (a) Cr<sup>6+</sup> and (b) Mn<sup>7+</sup>. Stern-Volmer (SV) plots of PANI/LDH@CNT nanocomposite for (c) Cr<sup>6+</sup> and (d) Mn<sup>7+</sup>.

Furthermore, the influence of some anions with and without Mn<sup>7+</sup> and Cr<sup>6+</sup> ions on the fluorescence quenching influence was investigated. In the existence of an anions' mixture (NO<sub>3</sub><sup>-</sup>, SO<sub>4</sub><sup>2-</sup>, CO<sub>3</sub><sup>2-</sup>), the sensitivity and selectivity of PANI/LDH@CNT for Cr<sup>6+</sup> and Mn<sup>7+</sup> ions detection were examined, and it was revealed that the FL intensity of PANI/LDH@CNT nanocomposite decreases by up to 39.4 % without adding Mn<sup>7+</sup> and Cr<sup>6+</sup>. The counter anions had a minor influence on detecting

Mn<sup>7+</sup> and Cr<sup>6+</sup> ions for PANI/LDH@CNT (Fig. 16a & b). Independently, the influence of anions (NO<sub>3</sub><sup>-</sup>, SO<sub>4</sub><sup>2-</sup>, CO<sub>3</sub><sup>2-</sup>) on Cr<sup>6+</sup> and Mn<sup>7+</sup> sensing was examined, as shown in Fig. 16c & d. As opposed to these co-existing anions, the FL intensity of PANI/LDH@CNT nanocomposite for 2 ppm Cr<sup>6+</sup> and Mn<sup>7+</sup> is markedly higher.

Additionally, we conducted FTIR, EDS morphological diagram, and EDS mapping analyses on PANI/LDH@CNT before and after Mn<sup>7+</sup> ion

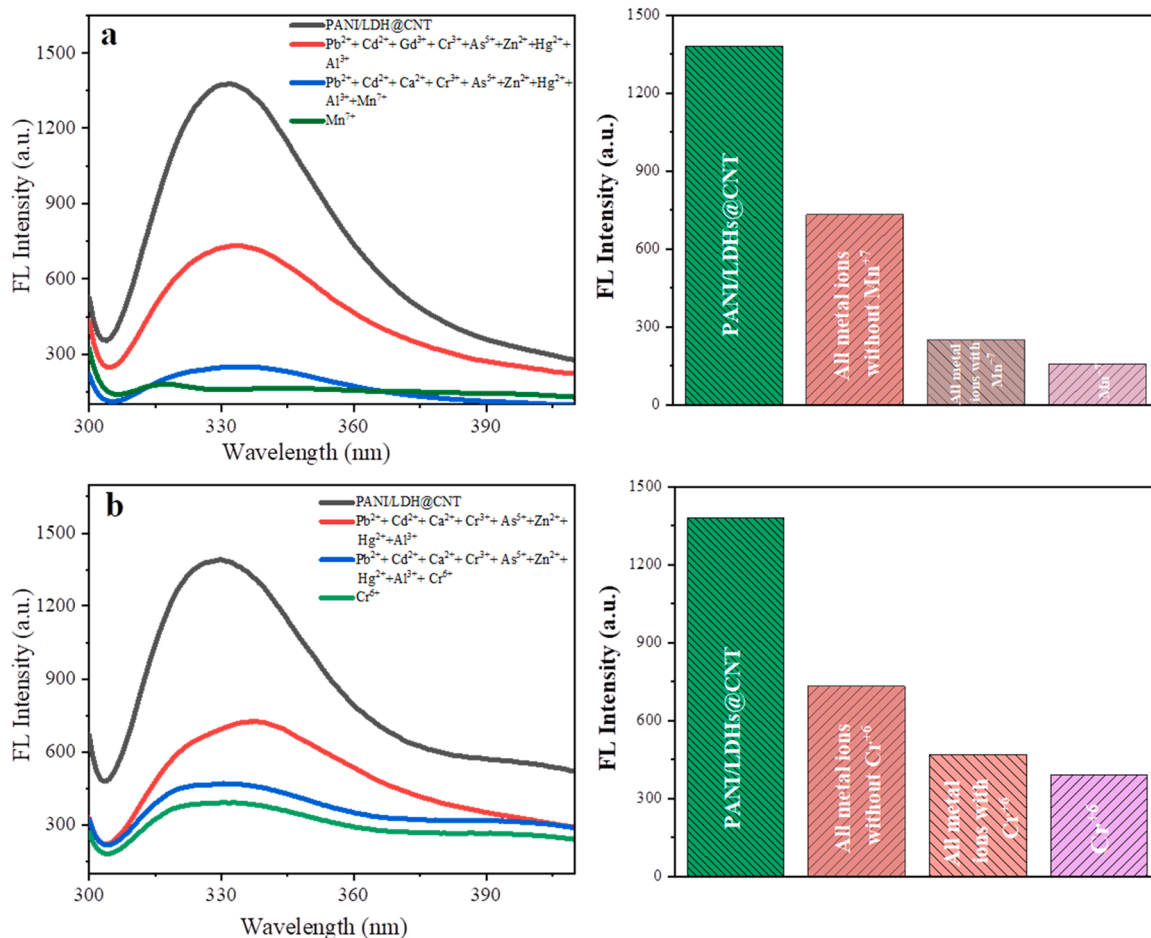


**Fig. 14.** Selective determination of (a)  $Mn^{7+}$  and (b)  $Cr^{6+}$  using PANI/LDH@CNT nanocomposite by comparison with various metal ions intensity of PANI/LDH@CNT.

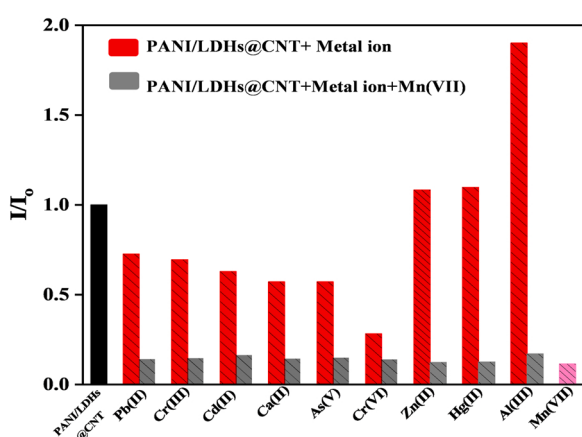


**Fig. 15.** Depicts the influence of interfering metal ions on the interaction of PANI/LDH@CNT with  $Mn^{7+}$  ions in aqueous solutions.  $Mn^{7+}$  ions and interfering metal ions in the suspensions at a concentration of 2 ppm. ( $\lambda_{ex} = 280$  nm).

sensing. When comparing the FTIR spectrums of PANI/LDH@CNT and PANI/LDH@CNT+ $Mn^{7+}$ , as shown in Fig. S11, there is just a difference in absorption intensity. Nonetheless, the placement of the peaks remained unchanged, showing that the PANI/LDH@CNT was preserved. Furthermore, the existence of  $Mn^{7+}$  in PANI/LDH@CNT after the quenching studies was also confirmed using EDS spectra (Fig. S12).

The IFE mechanism was used to detect  $Mn^{7+}$  and  $Cr^{6+}$  ions in aqueous solutions. The IFE is a non-irradiation energy conversion in which the excitation or emission wavelength of the adsorbent is quenched by the adsorbate. In IFE, the quencher's absorption band should complementarily overlap with the excitation or emission or with both bands of the fluorescent agent.  $Mn^{7+}$  shows one prominent absorption band centered at 354 nm, while  $Cr^{6+}$  shows two prominent absorption bands at 272 and 372 nm. In addition, the prepared nanomaterial PANI@NdLDH exhibits excitation and emission bands at 280 and 332 nm, respectively. The investigation of UV-Vis absorption for  $Mn^{7+}$  and  $Cr^{6+}$  indicates that the absorptions of  $Mn^{7+}$  and  $Cr^{6+}$  originate from a strong overlapping with the excitation and emission bands as shown in Fig. 17. Consequently, these ions can absorb the excitation and emission energy, decreasing luminescence intensities, and this might indicate energy-transfer processes for  $Mn^{7+}$  and  $Cr^{6+}$  fluorescence quenching [1].

### 3.6.3. Fluorescence "Turn-On" sensing of $Al^{3+}$ ion

The fluorescence titration for the binding of PANI/LDH@CNT with  $Al^{3+}$  was conducted in  $H_2O$  solution, where different concentrations of  $Al^{3+}$  in the range 0–450 ppb were investigated. Fig. 18a shows that the fluorescence intensity at 322 nm gradually rose with the rise of  $Al^{3+}$  concentration, even at a low concentration of 50 ppb, and may be attributed to the chelation-enhanced fluorescence (CHEF) effect. The photoinduced electron transfer (PET) mechanism governs the PANI/LDH@CNT- $Al^{3+}$  complex of a CHEF effect. Firstly, in the PET mechanism, electrons are stimulated in the free PANI/LDH@CNT by the exciting photons to migrate from the lone pairs on donor atoms, the like

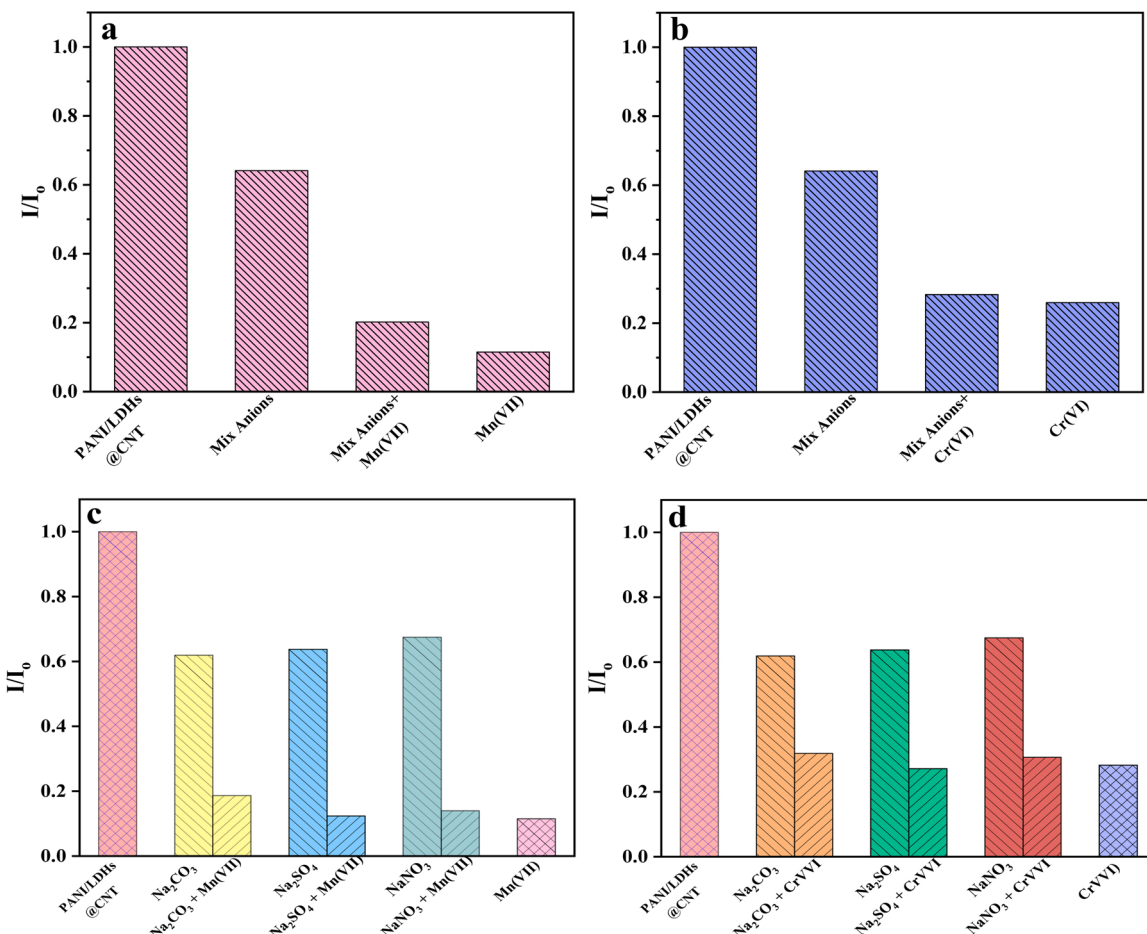


**Fig. 16.** (a & b) Effect of Mn<sup>7+</sup> and Cr<sup>6+</sup> on FL emission spectra of PANI/LDH@CNT nanocomposite in the existence of a mixture of anions (Na<sub>2</sub>SO<sub>4</sub>, Na<sub>2</sub>CO<sub>3</sub>, and NaNO<sub>3</sub>), (b) FL emission spectra of PANI/LDH@CNT nanocomposite in the existence of various anions (2 ppm for each) with and without Mn<sup>7+</sup> and Cr<sup>6+</sup>.

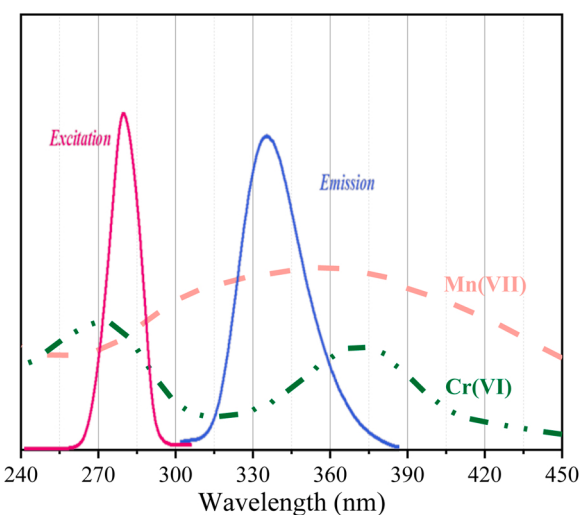


**Fig. 17.** UV-vis absorption spectra of Mn<sup>7+</sup> and Cr<sup>6+</sup> in aqueous solutions and the excitation and emission spectra of PANI/LDH@CNT nanocomposite.

of nitrogen, and oxygen atoms of fluorophores, thus leading to quenching fluorescence. In contrast, the existence of the coordinated Al<sup>3+</sup> ion in sensor PANI/LDH@CNT reduces the energy of the ion pair, eliminating the (PET) quenching activity and resulting in the CHEF effect. Thus the fluorescence intensity of the PANI/LDH@CNT was sensitive to the concentration change of Al<sup>3+</sup>, and Scheme 2 describes the

proposed binding mechanism [35,55,8,79].

As shown in Fig. 18b linear relationship between Al<sup>3+</sup> concentration and fluorescence intensity was observed in the range 50–450 ppb, and the value of R<sup>2</sup> was 0.994. The LOD for Al<sup>3+</sup> was determined using the 3σ method to be  $8.1 \times 10^{-8}$  M, which is significantly low by the recommended concentration of US EPA's (0.05–0.2 mg L<sup>-1</sup>) and WHO (0.2 mg L<sup>-1</sup>) drinking water standard [27] as well as outperforming several of the reported detecting methods (Table S3), indicating that MA-1 @CNT could be used as an excellent environmental sensor.

#### 4. Conclusion

To Summarize, the hybrid material (PANI/LDH@CNT) was synthesized by combining PANI, Pr-Co/LDH, and F-CNT materials through in-situ oxidative polymerization. This obtained nanomaterial contains abundant oxygen, sulfur, and nitrogen in its skeleton. Impressively, PANI/LDH@CNT works as a tremendous “turn-on” and “turn-off” sensor for Mn<sup>7+</sup> and Cr<sup>6+</sup> Al<sup>3+</sup> ions, which have serious health hazards. In this context, the fluorescence intensity of the PANI/LDH@CNT was turned off in the presence of Mn<sup>7+</sup> and Cr<sup>6+</sup> because of the IFE. In contrast, the fluorescence intensity was turned on in the case of Al<sup>3+</sup>, relying on the CHEF mechanism. On the other hand, PANI/LDH@CNT can uptake radioactive iodine, which is a significant environmental contamination source. Overall, this work provides useful information for creating multifunctional organic-inorganic hybrid composites, which can be used in toxic iodine adsorption and fluorescent metal ion detection.

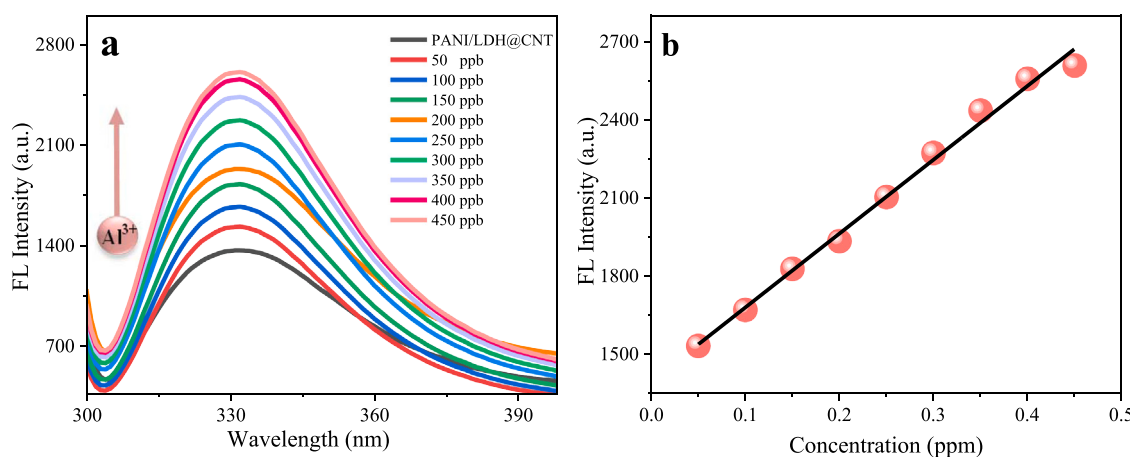
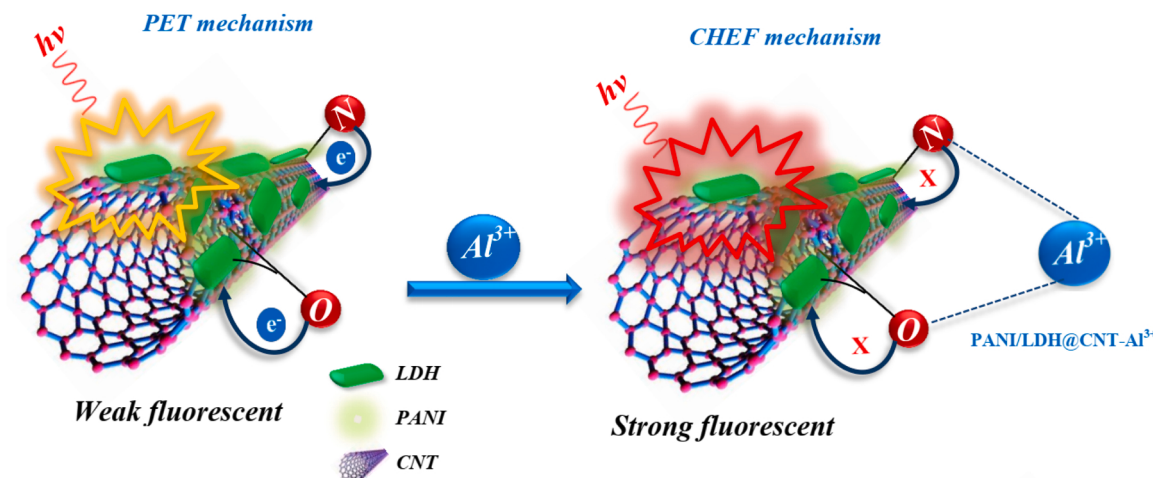


**Fig. 18.** (a) Changes in fluorescence intensity of PANI/LDH@CNT nanocomposite ( $\lambda_{\text{ex}} = 280 \text{ nm}$ ) in deionized water (0.3 mg/ mL), (pH= 7.0) at RT, upon incremental addition of  $\text{Al}^{3+}$  ion, and (b) Calculate LOD of PANI/LDH@CNT nanocomposite for  $\text{Al}^{3+}$ .



**Scheme 2.** The proposed mechanism of PANI/LDH@CNT for sensing  $\text{Al}^{3+}$ .

## Environmental implication

Widespread contamination of freshwater by toxic pollutants due to anthropogenic and biochemical activities has emerged as one of the world's most focused environmental issues. Among all toxic pollutants, heavy metal and radioactive iodine have been identified as the most harmful pollutant released into the environment, which causes devastating effects on most organisms, mainly aquatic life. The prepared PANI/LDH@CNT is probably the first example based on PANI/LDH@CNT as a multifunctional hybrid material that showed a practical approach as an adsorbent for capturing radioactive iodine and as a chemosensor for detecting heavy metal ions as  $\text{Mn}^{7+}$ ,  $\text{Cr}^{6+}$ , and  $\text{Al}^{3+}$  in aqueous solutions.

## CRediT authorship contribution statement

**Mansour A.S. Salem:** Conceptualization, Methodology, Investigation, Writing – original draft, Writing. **Amjad Mumtaz Khan:** Supervision, review & editing. **Yahiya Kadaf Manea:** Data curation, Visualization. **Mohsen T. A. Qashqoosh:** Software, Validation, and **Faiza A. M. Alahdal:** Methodology.

## Declaration of Competing Interest

The authors declare that they have no known competing financial interests or personal relationships that could have appeared to influence the work reported in this paper.

## Data availability

No data was used for the research described in the article.

## Acknowledgements

The authors would like to gratefully acknowledge the Department of Chemistry, University Sophisticated Instrument Facility (USIF), AMU, Aligarh for providing an instrumental facility.

## Appendix A. Supporting information

Supplementary data associated with this article can be found in the online version at doi:10.1016/j.jhazmat.2023.130732.

## References

- [1] Abdollahi, N., Morsali, A., 2019. Highly sensitive fluorescent metal-organic framework as a selective sensor of Mn VII and Cr VI anions ( $\text{MnO}_4^{4-}/\text{Cr}_2\text{O}_7^{2-}$

- /CrO 42-) in aqueous solutions. *Anal Chim Acta* 1064, 119–125. <https://doi.org/10.1016/j.jaca.2019.02.061>.
- [2] Abdolmohammad-Zadeh, H., Sadeghi, G.H., 2012. A nano-structured material for reliable speciation of chromium and manganese in drinking waters, surface waters and industrial wastewater effluents. *Talanta* 94, 201–208. <https://doi.org/10.1016/J.TALANTA.2012.03.022>.
- [3] Ahmad, A., et al., 2021. Selective adsorption and ultrafast fluorescent detection of Cr (VI) in wastewater using neodymium doped polyaniline supported layered double hydroxide nanocomposite. *J Hazard Mater* 416, 125754. <https://doi.org/10.1016/j.jhazmat.2021.125754>.
- [4] Al Lafi, A.G., Assfour, B., Assaad, T., 2020. Metal organic framework MIL-101(Gr): spectroscopic investigations to reveal iodine capture mechanism. *J Inorg Organomet Polym Mater* 30 (4), 1218–1230. <https://doi.org/10.1007/s10904-019-01236-7>.
- [5] Alahdal, F.A.M., Qashqoosh, M.T.A., Manea, Y.K., et al., 2022. Eco-friendly synthesis of zinc oxide nanoparticles as nanosensor, nanocatalyst and antioxidant agent using leaf extract of *P. austroarabica*. *OpenNano* 8, 100067. <https://doi.org/10.1016/J.ONANO.2022.100067>.
- [6] Alahdal, F.A.M., Qashqoosh, M.T.A., Kadaf Manea, Y., et al., 2022. Ultrafast fluorescent detection of hexavalent chromium ions, catalytic efficacy and antioxidant activity of green synthesized silver nanoparticles using leaf extract of *P. austroarabica*. *Environ Nanotechnol Monit Manag* 17, 100665. <https://doi.org/10.1016/j.enmm.2022.100665>.
- [7] Amini, R., Rahimpour, E., Jouyban, A., 2020. An optical sensing platform based on hexacyanoferrate intercalated layered double hydroxide nanozyme for determination of chromium in water. *Anal Chim Acta* 1117, 9–17. <https://doi.org/10.1016/j.jaca.2020.04.001>.
- [8] Amirmasr, M., Sadeghi Erami, R., Meghdadi, S., 2016. A fluorescent carboxamide ligand, having combined ionophore/fluorophore moieties, exhibiting “On-Off” switching toward Zn<sup>2+</sup> ion. *Sens Actuators B Chem* 233, 355–360. <https://doi.org/10.1016/j.snb.2016.04.077>.
- [9] Andersen, O., 1999. Principles and recent developments in chelation treatment of metal intoxication. *Chem Rev* 99 (9), 2683–2710. <https://doi.org/10.1021/CR980453A>.
- [10] Asmussen, R.M., et al., 2019. Silver-functionalized silica aerogels and their application in the removal of iodine from aqueous environments. *J Hazard Mater* 379, 119364. <https://doi.org/10.1016/J.JHAZMAT.2018.04.081>.
- [11] Benselika-Hadj Abdelkader, N., et al., 2011. Synthesis and characterization of Mg-Fe layer double hydroxides and its application on adsorption of Orange G from aqueous solution. *Chem Eng J* 169 (1–3), 231–238. <https://doi.org/10.1016/j.cej.2011.03.019>.
- [12] Bugatti, V., et al., 2020. Ionic liquid as dispersing agent of LDH-carbon nanotubes into a biodegradable vinyl alcohol polymer. *Polymers* 12 (2), 495. <https://doi.org/10.3390/POLYM12020495>.
- [13] Bugatti, V. et al. (no date) Ionic liquid as dispersing agent of ldh-carbon nanotubes into a biodegradable vinyl alcohol polymer. Available from: doi: [10.3390/polymer12020495](https://doi.org/10.3390/polymer12020495).
- [14] Cao, X., et al., 2019. Facile fabrication of the polyaniline/layered double hydroxide nanosheet composite for supercapacitors. *Appl Clay Sci* 168, 175–183. <https://doi.org/10.1016/j.jclay.2018.11.011>.
- [15] Chen, G., et al., 2022. Pitch-based porous polymer beads for highly efficient iodine capture. *J Hazard Mater* 434, 128859. <https://doi.org/10.1016/J.JHAZMAT.2022.128859>.
- [16] Chen, J., et al., 2020. Enhanced removal of I<sup>-</sup> on hierarchically structured layered double hydroxides by in situ growth of Cu/Cu<sub>2</sub>O. *J Environ Sci* 88, 338–348. <https://doi.org/10.1016/J.JES.2019.09.024>.
- [17] Chen, Y., et al., 2014. The dynamic process of radioactive iodine removal by ionic liquid 1-butyl-3-methyl-imidazolium acetate: discriminating and quantifying halogen bonds versus induced force. *RSC Adv* 4 (98), 55417–55429. <https://doi.org/10.1039/C4RA06096E>.
- [18] Dai, K., et al., 2013. Hydrothermal synthesis of single-walled carbon nanotube-TiO<sub>2</sub> hybrid and its photocatalytic activity. *Appl Surf Sci* 270, 238–244. <https://doi.org/10.1016/j.apsusc.2013.01.010>.
- [19] Das, T., et al., 2017. 2-Hydroxy-naphthal functionalized mesoporous silica for fluorescence sensing and removal of aluminum ions. *Dalton Trans* 46 (22), 7317–7326. <https://doi.org/10.1039/C7DT00369B>.
- [20] Diao, Z., et al., 2021. A new insight on enhanced Pb (II) removal by sludge biochar catalyst coupling with ultrasound irradiation and its synergism with phenol removal. *Chemosphere* 263, 128287. <https://doi.org/10.1016/j.chemosphere.2020.128287>.
- [21] Dutta, K., Deka, R.C., Das, D.K., 2013. A new on-fluorescent probe for manganese (II) ion. *J Fluoresc* 23 (6), 1173–1178. <https://doi.org/10.1007/S10895-013-1248-0>.
- [22] El-Absy, M.A., et al., 2010. Separation and purification of 131I from neutron irradiated tellurium dioxide targets by wet-distillation method. *Sep Purif Technol* 71 (1), 1–12. <https://doi.org/10.1016/J.SEPPUR.2009.06.008>.
- [23] González, M.A., Pavlovic, I., Barriga, C., 2015. Cu(II), Pb(II) and Cd(II) sorption on different layered double hydroxides. A kinetic and thermodynamic study and competing factors. *Chem Eng J* 269 (II), 221–228. <https://doi.org/10.1016/j.cej.2015.01.094>.
- [24] Harijan, D.K.L., et al., 2018. Radioactive iodine capture and storage from water using magnetite nanoparticles encapsulated in polypyrrole. *J Hazard Mater* 344, 576–584. <https://doi.org/10.1016/j.jhazmat.2017.10.065>.
- [25] Hasell, T., Schmidtmann, M., Cooper, A.I., 2011. Molecular doping of porous organic cages. *J Am Chem Soc* 133 (38), 14920–14923. <https://doi.org/10.1021/JA205969Q> SUPPL\_FILE/JA205969Q\_SI\_012.PDF.
- [26] Huang, Y., et al., 2021. Rapid iodine adsorption from vapor phase and solution by a nitrogen-rich covalent pipеразине-triazine-based polymer. *New J Chem* 45 (12), 5363–5370. <https://doi.org/10.1039/d1nj00122a>.
- [27] Izabela Krupinska, 2020. Aluminum drinking water treatment residuals and their toxic impact on human health. *Molecules* 25 (3), 13.
- [28] Jaiswal, A., et al., 2015. Synthesis of novel nano-layered double hydroxide by urea hydrolysis method and their application in removal of chromium(VI) from aqueous solution: kinetic, thermodynamic and equilibrium studies. *J Mol Liq* 202, 52–61. <https://doi.org/10.1016/j.molliq.2014.12.004>.
- [29] Jiang, M., et al., 2022. Novel synthesis of NaY-NH4F-Bi2S3 composite for enhancing iodine capture. *Chem Eng J* 443, 136477. <https://doi.org/10.1016/J.CEJ.2022.136477>.
- [30] Kamal, S., et al., 2022. Amine- and imine-functionalized Mn-based MOF as an unusual turn-on and turn-off sensor for d10 heavy metal ions and an efficient adsorbent to capture iodine. *Cryst Growth Des* 22 (5), 3277–3294. <https://doi.org/10.1021/acs.cgd.2c0092>.
- [31] Kang, K., et al., 2021. Unveiling the uncommon fluorescent recognition mechanism towards pertechnetate using a cationic metal-organic framework bearing N-Heterocyclie AIE molecules. *Chem Eur J* 27 (18), 5632–5637. <https://doi.org/10.1002/CHEM.202005362>.
- [32] Kim, S.H., et al., 2010. Novel optical/electrochemical selective 1,2,3-triazole ring-appended chemosensor for the Al<sup>3+</sup> ion. *Org Lett* 12 (3), 560–563. <https://doi.org/10.1021/OL902743S> SUPPL\_FILE/OL902743S\_SI\_001.PDF.
- [33] Kitada, S., et al., 2014. Removal of radioactive iodine and cesium in water purification. *New Pub Balaban* 54 (13), 3494–3501. <https://doi.org/10.1080/19443994.2014.923205>.
- [34] Kosaka, K., et al., 2012. Removal of radioactive iodine and cesium in water purification processes after an explosion at a nuclear power plant due to the Great East Japan earthquake. *Water Res* 46 (14), 4397–4404. <https://doi.org/10.1016/J.WATRES.2012.05.055>.
- [35] Kouuser, R., et al., 2021. “Turn-on” benzophenone based fluorescence and colorimetric sensor for the selective detection of Fe<sup>2+</sup> in aqueous media: validation of sensing mechanism by spectroscopic and computational studies. *Spectrochim Acta Part A Mol Biomol Spectrosc* 247, 119156. <https://doi.org/10.1016/j.saa.2020.119156>.
- [36] Li, Y., et al., 2012. Carbon nanotube/titania composites prepared by a micro-emulsion method exhibiting improved photocatalytic activity. *Appl Catal A Gen* 427–428, 1–7. <https://doi.org/10.1016/J.APCATA.2012.03.004>.
- [37] Liao, S., et al., 2015. Simultaneous separation of iodide and cesium ions from dilute wastewater based on PPy/PTCF and NiHCF/PTCF electrodes using electrochemically switched ion exchange method. *Sep Purif Technol* 139, 63–69. <https://doi.org/10.1016/J.SEPPUR.2014.11.003>.
- [38] Liao, Y., et al., 2016. Highly efficient and reversible iodine capture in hexaphenylbenzene-based conjugated microporous polymers. *Macromolecules* 49 (17), 6322–6333. <https://doi.org/10.1021/acs.macromol.6b00901>.
- [39] Liao, Y., et al., 2016. Highly efficient and reversible iodine capture in hexaphenylbenzene-based conjugated microporous polymers. *Macromolecules* 49 (17), 6322–6333. [https://doi.org/10.1021/ACS.MACROMOL.6B00901/ASSET IMAGES/LARGE/MA-2016-00901\\_0011.JPG](https://doi.org/10.1021/ACS.MACROMOL.6B00901/ASSET IMAGES/LARGE/MA-2016-00901_0011.JPG).
- [40] Liu, L., et al., 2019. Preparation of NiCoFe-hydroxide/polyaniline composite for enhanced-performance supercapacitors. *J Mater Sci Technol* 35 (8), 1691–1699. <https://doi.org/10.1016/j.jmst.2019.04.003>.
- [41] Maity, D., Manoharan, M., Rajendra Kumar, R.T., 2020. Development of the PANI/MWCNT nanocomposite-based fluorescent sensor for selective detection of aqueous ammonia. *ACS Omega* 5 (15), 8414–8422. <https://doi.org/10.1021/acsomega.9b02885>.
- [42] Mallakpour, S., Hatami, M., 2017. Condensation polymer/layered double hydroxide NCs: preparation, characterization, and utilizations. *Eur Polym J*. <https://doi.org/10.1016/J.EURPOLYMJ.2017.03.015>.
- [43] Manea, Y.K., et al., 2021. Hydrothermally synthesized mesoporous CS-g-PA@TSM functional nanocomposite for efficient photocatalytic degradation of Ciprofloxacin and treatment of metal ions. *J Mol Liq* 335, 116144. <https://doi.org/10.1016/J.MOLLIQ.2021.116144>.
- [44] Manea, Y.K., et al., 2022. In-grown flower like Al-Li/Th-LDH@CNT nanocomposite for enhanced photocatalytic degradation of MG dye and selective adsorption of Cr (VI). *J Environ Chem Eng* 10 (1), 106848. <https://doi.org/10.1016/J.JECE.2021.106848>.
- [45] Mathai, C.J., et al., 2002. Effect of iodine doping on the bandgap of plasma polymerized aniline thin films. *J Phys D Appl Phys* 35 (17), 2206. <https://doi.org/10.1088/0022-3727/35/17/318>.
- [46] Michalke, B., Fernsebner, K., 2014. New insights into manganese toxicity and speciation. *J Trace Elem Elelmt Biol* 28 (2), 106–116. <https://doi.org/10.1016/J.JTEMB.2013.08.005>.
- [47] Mostafa, M.S., et al., 2016. Water decontamination via the removal of Pb (II) using a new generation of highly energetic surface nano-material: Co<sub>2</sub>Mo<sub>6</sub>+ LDH. *J Colloid Interface Sci* 461, 261–272. <https://doi.org/10.1016/J.JCIS.2015.08.060>.
- [48] Moyo, M., et al., 2014. Kinetic and equilibrium modelling of lead sorption from aqueous solution by activated carbon from goat dung. *New Pub Balaban* 57 (2), 765–775. <https://doi.org/10.1080/19443994.2014.968217>.
- [49] Mu, W., et al., 2017. Niobate nanofibers for simultaneous adsorptive removal of radioactive strontium and iodine from aqueous solution. *J Alloy Compd* 693, 550–557. <https://doi.org/10.1016/J.JALLCOM.2016.09.200>.
- [50] Mushtaq, S., et al., 2017. Efficient and selective removal of radioactive iodine anions using engineered nanocomposite membranes. *Environ Sci Nano* 4 (11), 2157–2163. <https://doi.org/10.1039/C7EN00759K>.

- [51] Nabieyan, B., et al., 2007. Bench-scale pertraction of iodine using a bulk liquid membrane system. Desalination 214 (1–3), 167–176. <https://doi.org/10.1016/J.DESAL.2006.08.018>.
- [52] Nandanwar, S.U., et al., 2017. Adsorption of radioactive iodine and krypton from off-gas stream using continuous flow adsorption column. Chem Eng J 320 (C), 222–231. <https://doi.org/10.1016/J.CEJ.2017.03.020>.
- [53] Naushad, M., Ahamad, T., Al-Sheetan, K.M., 2021. Development of a polymeric nanocomposite as a high performance adsorbent for Pb(II) removal from water medium: Equilibrium, kinetic and antimicrobial activity. J Hazard Mater. <https://doi.org/10.1016/j.jhazmat.2020.124816>.
- [54] Normandin, L., Hazell, A.S., 2002. Manganese neurotoxicity: an update of pathophysiological mechanisms. Metab Brain Dis 17 (4), 375–387. <https://doi.org/10.1023/A:1021970120965>.
- [55] Pal, S., et al., 2015. Selective and sensitive turn-on chemosensor for Al(iii) ions applicable in living organisms: nanomolar detection in aqueous medium. RSC Adv 5 (89), 72508–72514. <https://doi.org/10.1039/c5ra13478a>.
- [56] Pan, X., et al., 2020. Adsorption behavior and mechanism of acid orange 7 and methylene blue on self-assembled three-dimensional MgAl layered double hydroxide: Experimental and DFT investigation. Appl Surf Sci 522 (April), 146370. <https://doi.org/10.1016/j.apsusc.2020.146370>.
- [57] Puglisi, R., et al., 2021. A facile one-pot approach to the synthesis of gd-eu based metal-organic frameworks and applications to sensing of fe<sup>3+</sup> and cr<sub>2</sub>o<sub>7</sub><sup>2-</sup> ions. Sensors 21 (5), 1–14. <https://doi.org/10.3390/s21051679>.
- [58] Qiao, L., et al., 2022. Mechanical properties, melting and crystallization behaviors, and morphology of carbon nanotubes/continuous carbon fiber reinforced polyethylene terephthalate composites. Polymers 14 (14). <https://doi.org/10.3390/POLYM14142892>.
- [59] Salem, M.A.S., et al., 2022. Nano chromium embedded in f-CNT supported CoBi-LDH nanocomposites for selective adsorption of Pb<sup>2+</sup> and hazardous organic dyes. Chemosphere 289, 133073. <https://doi.org/10.1016/j.chemosphere.2021.133073>.
- [60] Salem, M.A.S., Khan, A.M., Manea, Y.K., 2022. A novel nano-hybrid carbon architecture as chemo sensor for natural hazards: active adsorption of Rose Bengal dye and detection of hazard pollutants at ppb level. J Environ Chem Eng 10 (1), 107032. <https://doi.org/10.1016/j.jece.2021.107032>.
- [61] Sankar, K.V., Selvan, R.K., 2015. The ternary MnFe2O4/graphene/polyaniline hybrid composite as negative electrode for supercapacitors. J Power Sources 275, 399–407. <https://doi.org/10.1016/j.jpowsour.2014.10.183>.
- [62] Svensson, P.H., Kloo, L., 2003. Synthesis, structure, and bonding in polyiodide and metal iodide-iodine systems. Chem Rev 103 (5), 1649–1684. <https://doi.org/10.1021/cr0204101>.
- [63] Tian, Z., et al., 2021. Comprehensive comparison of bismuth and silver functionalized nickel foam composites in capturing radioactive gaseous iodine. J Hazard Mater 417, 125978. <https://doi.org/10.1016/J.JHAZMAT.2021.125978>.
- [64] Tian, Z., et al., 2022. Incipient wetness impregnation to prepare bismuth-modified all-silica beta zeolite for efficient radioactive iodine capture. Environ Funct Mater 1 (1), 92–104. <https://doi.org/10.1016/J.EFMAT.2022.05.006>.
- [65] Wakshe, Saubai B., et al., 2021. A highly sensitive and selective phthalazine derivative based fluorescent organic nanosheets for simultaneous detection of Cr<sup>6+</sup> and Mn<sup>7+</sup> in aqueous media. Inorg Chim Acta 526, 120534. <https://doi.org/10.1016/J.ICA.2021.120534>.
- [66] Wakshe, Saubai B., et al., 2021. A highly sensitive and selective phthalazine derivative based fluorescent organic nanosheets for simultaneous detection of Cr<sup>6+</sup> and Mn<sup>7+</sup> in aqueous media. Inorg Chim Acta 526 (July), 120534. <https://doi.org/10.1016/j.ica.2021.120534>.
- [67] Wang, B., et al., 2010. Effects of chronic aluminum exposure on memory through multiple signal transduction pathways. Environ Toxicol Pharmacol 29 (3), 308–313. <https://doi.org/10.1016/J.ETAP.2010.03.007>.
- [68] Wang, J., et al., 2021. Synthesis of cnts/conife-ldh nanocomposite with high specific surface area for asymmetric supercapacitor. Nanomaterials 11 (9). <https://doi.org/10.3390/nano11092155>.
- [69] Wang, Q., et al., 2022. Keggin-type polycationic AlO<sub>4</sub>Al<sub>12</sub>(OH)<sub>24</sub>(H<sub>2</sub>O)<sub>127+</sub>-intercalated MoO<sub>3</sub> composites for methyl orange adsorption. Chin Chem Lett 33 (5), 2617–2620. <https://doi.org/10.1016/J.CCLT.2021.09.079>.
- [70] Wang, S., et al., 2022. Two-dimensional assembly made up of ZIF-8 particles for the high-efficient capture of the iodine and dyes. J Hazard Mater 430, 128501. <https://doi.org/10.1016/J.JHAZMAT.2022.128501>.
- [71] Wani, A.A., Khan, A.M., Manea, Y.K., Salem, M.A.S., 2021. Enhanced photocatalytic degradation of organic dyes from aqueous environment using neodymium-doped mesoporous layered double hydroxide. J Rare Earths. <https://doi.org/10.1016/J.JRE.2021.09.007>.
- [72] Wani, A.A., Khan, A.M., Manea, Y.K., Salem, M.A.S., et al., 2021. Selective adsorption and ultrafast fluorescent detection of Cr(VI) in wastewater using neodymium doped polyaniline supported layered double hydroxide nanocomposite. J Hazard Mater 416, 125754. <https://doi.org/10.1016/J.JHAZMAT.2021.125754>.
- [73] Xu, H., et al., 2021. Rapid and efficient removal of diclofenac sodium from aqueous solution via ternary core-shell CS @ PANI @ LDH composite: experimental and adsorption mechanism study. J Hazard Mater 402 (June 2020), 123815. <https://doi.org/10.1016/j.jhazmat.2020.123815>.
- [74] Yan, Z., et al., 2021. A carbazole-functionalized porous aromatic framework for enhancing volatile iodine capture via lewis electron pairing. Molecules 26 (17). <https://doi.org/10.3390/MOLECULES26175263>.
- [75] Yang, W., et al., 2021. Smart mn<sup>7+</sup> sensing via quenching on dual fluorescence of eu<sup>3+</sup> complex-modified tio<sub>2</sub> nanoparticles. Nanomaterials 11 (12). <https://doi.org/10.3390/nano11123283>.
- [76] Yazdi, M.K., et al., 2019. PANI-CNT nanocomposites. Fundamentals and Emerging Applications of Polyaniline. Elsevier Inc., <https://doi.org/10.1016/B978-0-12-817915-4.00009-9>.
- [77] Yu, F., et al., 2020. Synthesis of metal-organic framework nanocrystals immobilized with 3D flowerlike Cu-Bi-layered double hydroxides for iodine efficient removal. J Mater Res 35 (3), 299–311. <https://doi.org/10.1557/JMR.2020.1>.
- [78] Zarejoushghani, M., et al., 2021. Molecularly imprinted polymer-based sensors for priority pollutants. Sensors 21 (7), 1–23. <https://doi.org/10.3390/s21072406>.
- [79] Zhang, S., et al., 2018. A dual-responsive colorimetric and fluorescent chemosensor based on diketopyrrolopyrrole derivative for naked-eye detection of Fe<sup>3+</sup> and its practical application. Spectrochim Acta - Part A Mol Biomol Spectrosc 189, 594–600. <https://doi.org/10.1016/j.saa.2017.09.001>.
- [80] Zhang, T., et al., 2012. Synthesis of Li-Al layered double hydroxides (LDHs) for efficient fluoride removal. Ind Eng Chem Res 51 (35), 11490–11498. <https://doi.org/10.1021/IE300863X>.
- [81] Zhang, Y., et al., 2021. Microwave hydrothermal fabrication of CuFeCr ternary layered double hydroxides with excellent Cr (VI) adsorption. Colloid Surf A Physicochem Eng Asp 628, 127279. <https://doi.org/10.1016/j.colsurfa.2021.127279>.
- [82] Zhu, K., et al., 2016. Polyaniline-modified Mg/Al layered double hydroxide composites and their application in efficient removal of Cr(VI). ACS Sustain Chem Eng 4 (8), 4361–4369. <https://doi.org/10.1021/acssuschemeng.6b00922>.
- [83] Zou, J.Y., et al., 2018. Two luminescent lanthanide(iii) metal-organic frameworks as chemosensors for high-efficiency recognition of Cr(vi) anions in aqueous solution. Dalton Trans 47 (44), 15694–15702. <https://doi.org/10.1039/C8DT03050B>.